Lawrence Livermore National Laboratory

Additively Manufactured Uranium-6 wt. pct. Niobium

Unclassified

September 29, 2017

Disclaimer

This document was prepared as an account of work sponsored by an agency of the United States government. Neither the United States government nor Lawrence Livermore National Security, LLC, nor any of their employees makes any warranty, expressed or implied, or assumes any legal liability or responsibility for the accuracy, completeness, or usefulness of any information, apparatus, product, or process disclosed, or represents that its use would not infringe privately owned rights. Reference herein to any specific commercial product, process, or service by trade name, trademark, manufacturer, or otherwise does not necessarily constitute or imply its endorsement, recommendation, or favoring by the United States government or Lawrence Livermore National Security, LLC. The views and opinions of authors expressed herein do not necessarily state or reflect those of the United States government or Lawrence Livermore National Security, LLC, and shall not be used for advertising or product endorsement purposes.

Lawrence Livermore National Laboratory is operated by Lawrence Livermore National Security, LLC, for the U.S. Department of Energy, National Nuclear Security Administration under Contract DE-AC52-07NA27344.

LLNL-TR-739064
Issued: 9/28/17
Approved for public release;
distribution is unlimited.

Additively Manufactured Uranium-6 wt. pct. Niobium

A. S. Wu
M. W. Wraith
S. C. Burke
A. V. Hamza
J. W. Elmer
J. T. McKeown
D. W. Brown (Los Alamos National Laboratory)
B. Clausen (Los Alamos National Laboratory)
L. L. Hsiung
R. E. Lindvall
E. M. Sedillo
N. E. Teslich
S. G. Torres
D. S. Urabe
D. C. Freeman
P. A. Alexander
M. R. Iniguez
F. J. Ryerson
D. S. Ancheta
J. P. Lotscher
E. W. Young
C. L. Evans
J. N. Florando
G. F. Gallegos
M. Marggraff
C. A. Hrousis
G. H. Campbell

Acknowledgements

This work was performed under the auspices of the U.S. Department of Energy by Lawrence Livermore National Laboratory under Contract DE-AC52-07NA27344, and has benefited from the use of the Lujan Neutron Scattering Center at LANSCE, which is funded by the National Nuclear Security Administration.

The authors gratefully acknowledge Robert Hackenberg (Los Alamos National Laboratory) for his expertise and guidance throughout this effort and for reviewing this report. The collaboration and expertise provided by Amy Clarke (Colorado School of Mines), Robert Aikin (Los Alamos National Laboratory), James Foley (Los Alamos National Laboratory), Roland Seals (Y-12 National Security Complex), Amy DeMint (Y-12 National Security Complex), Robert Bridges (Y-12 National Security Complex) and Jeffrey Cook (Y-12 National Security Complex) has been instrumental in guiding this effort. The authors are grateful to Derek Wapman for program funding and support, Daniel Haylett for physics expertise, Thomas Pluschkell for additive manufacturing and powder expertise, Rod Coleman and Nicholas Stankovich for material management, Mark Pearson for powder sieving and preparation, Jackson Go for metallurgical specimen preparation, John Karle for specimen machining and Dennis Wilson and Glenn Smith for wire electrical discharge machining.

Table of Contents

Section 1. Introductory Comments 1
Section 2. Additively Manufactured U-6Nb Specimen Preparation 3
2.1 Precursor powder 3
2.2 Laser powder bed fusion processing 4
2.3 Specimen machining 4
2.4 Solutionization and annealing heat treatments 5
Section 3. Composition and Crystallography 7
3.1 Bulk metallic composition 7
3.2 Effect of AM on metallic composition 7
3.3 Crystallography 8
Section 4. Oxidation and Nonmetallic Impurities 10
4.1 Impurity content 10
4.2 Impurity form 12
Section 5. Microstructure 14
5.1 As built microstructure 14
5.2 Effect of post build heat treatment on microstructure 16
5.2.1 Grain size 16
5.2.2 Inclusions 17
Section 6. Mechanical Behavior and Failure Analysis 22
6.1 Quasi-static tensile testing 22
6.2 Deformation behavior 23
6.3 Failure analysis 24
Section 7. Summary 27
Appendix A. References 28

Table of Figures

Figure 1. Scanning electron micrographs of pre-alloyed U-6Nb powder imaged at 5 keV via secondary electrons....3
Figure 2. Particle size distribution from sieve analysis on two samplings, 200 g each, of U-6Nb powder....4
Figure 3. Tensile bar photo and schematic (dimensions provided in inches); conical ends accommodate self-alignment in the tapered grips....5
Figure 4. Lattice constant evolution during a 1000ºC hold measured via in situ neutron diffraction....6
Figure 5. Niobium diffusion distance in uranium, plotted at 840ºC and 1000ºC, with selected heat treatments indicated in blue and orange, determined using D_0=1.5 (10^{-4}) cm^2/s and Q=33 kcal/mol [5, 43]....6
Figure 6. Uranium and niobium detected in two powder samples and three randomly selected AM samples, measurements via ICP-MS.....8
Figure 7. Diffraction patterns from U-6Nb for the Powder 2 material (described in Table 1 and 2) in: a) powder, b) as-built, and c) homogenized/WQ condition....9
Figure 8. Nonmetallic impurity content in µg/g measured using IGF; note that the oxygen values shown in the powder specimens were provided by the powder manufacturer.....10
Figure 9. Oxygen level in each Ti-6Al-4V specimen built using the Concept Laser M2 [51]....11
Figure 10. Neutron diffraction spectra of two powder samples, builds and one HT build, acquired via SMARTS diffractometer....12
Figure 11. Oxide particles observed in an AM build via transmission electron microscopy [52]....13
Figure 12. Melt pool structure observed at a 45º cross-section of an as built AM U-6Nb specimen imaged via optical microscopy....14
Figure 13. Higher magnification images depicting the melt pool structure observed at a 45º cross-section of an as built AM U-6Nb specimen imaged via optical microscopy....15
Figure 14. Solidification cells observed at a 45º cross-section in an as built AM U-6Nb specimen imaged via scanning electron microscopy at 5 kV (a) lower and (b) higher magnification....15
Figure 15. Microstructure of AM U-6Nb specimens annealed at (a) 840ºC for 6h and WQ and (b) 1000ºC for 16h, followed by a 30 min hold at 840ºC and WQ. Optical images of polished and etched surfaces.....16
Figure 16. Transmission electron micrographs depicting finely twinned laths or bands. High-angle annular dark field scanning TEM (left) and conventional bright field imaging (right).....16
Figure 17. Optical micrograph of an AM U-6Nb specimens annealed at 1000ºC for 16h, followed by a 30 min hold at 840ºC and WQ....17
Figure 18. Scanning electron micrographs of an AM U-6Nb specimen annealed at 1000ºC for 16h, followed by a 30 min hold at 840ºC and WQ, imaged at 5 keV via secondary electrons....17
Figure 19. Scanning electron micrographs depicting EDS regions on an AM U-6Nb specimen annealed at 1000ºC for 16h, followed by a 30 min hold at 840ºC and WQ, imaged at 5 keV via secondary electrons....18
Figure 20. Scanning electron micrographs depicting inclusions and their cross-sections observed in an AM U-6Nb specimen annealed at 1000ºC for 16h, followed by a 30 min hold at 840ºC and WQ, imaged at 5 keV via secondary electrons. (a) Image showing section locations, (b) cross-section 1, (c) cross-section 2....19
Figure 21. Inclusions shown in (a) an AM HT1 build and (b) an AM HT2 build, imaged at 5 keV via secondary electrons....20
Figure 22. Inclusions present in an AM build after annealing at 1000ºC for 16h, followed by a 30 min hold at 840ºC and WQ....20
Figure 23. EDS mapping acquired in the TEM chamber across the rod-like precipitate, matrix and surface layer....21
Figure 24. Quasi-static tensile engineering stress-strain behavior of AM U-6Nb specimens annealed at different time/temperatures.....22
Figure 25. Quasi-static tensile response of AM U-6Nb, shown in comparison with wrought processed U-6Nb [58]23

Figure 26. Fracture surface of (a) AM TB1 in the as built condition, (b) AM TB2 in the 840ºC 6h HT WQ condition and (c) AM TB3 in the 1000ºC 16h HT WQ condition acquired using scanning electron microscopy, E-SEM, 30 kV 23
Figure 27. Electron micrographs acquired via E-SEM, 30 kV, of the failure surface of an AM U-6Nb specimen tested in the AB condition 24
Figure 28. Electron micrographs acquired via E-SEM, 30 kV, of the failure surface of an AM U-6Nb specimen tested in the HT1 condition.....24
Figure 29. Electron micrographs acquired via E-SEM, 30 kV, of the failure surface of an AM U-6Nb specimen tested in the HT2 condition.....25
Figure 30. Higher magnification electron micrographs acquired via E-SEM, 30 kV, of the failure surface of an AM U-6Nb specimen tested in the AB condition 25
Figure 31. Higher magnification electron micrographs acquired via E-SEM, 30 kV, of the failure surface of an AM U-6Nb specimen tested in the HT1 condition.....26
Figure 32. Higher magnification electron micrographs acquired via E-SEM, 30 kV, of the failure surface of an AM U-6Nb specimen tested in the HT2 condition.....26

Table of Tables

Table 1. Concentration of impurities in the U-6Nb powder 1 and powder 2; measurement made via ionically coupled plasma mass spectroscopy (ICP-MS). All measurements are in µg/g, unless otherwise indicated. 2
Table 2. Concentration of impurities in the U-6Nb powder and U-6Nb specimens after powder bed fusion processing measured via ICP-MS. All compositions are in µg/g unless otherwise noted. 7
Table 3. Composition measured via uncalibrated EDS in at% for regions 1-3, specified in Fig. 18 18
Table 4. Composition in a rod-like inclusion measured via EDS in the TEM chamber, shown in at%. 21

Abstract

This report describes an effort to process uranium-6 weight% niobium using laser powder bed fusion. The chemistry, crystallography, microstructure and mechanical response resulting from this process are discussed with particular emphasis on the effect of the laser powder bed fusion process on impurities. In an effort to achieve homogenization and uniform mechanical behavior from different builds, as well as to induce a more conventional loading response, we explore post-processing heat treatments on this complex alloy. Elevated temperature heat treatment for recrystallization is evaluated and the effect of recrystallization on mechanical behavior in laser powder bed fusion processed U-6Nb is discussed. Wrought-like mechanical behavior and grain sizes are achieved through post-processing and are reported herein.

Section 1

Introductory Comments

Uranium alloyed with 6 wt. pct. niobium (U-6Nb) offers high density and good corrosion resistance to industrial sectors including nuclear fuels [1], storage containers for nuclear waste [2], ballasts and counterweights for aircraft [3] and defense applications, such as armor-piercing munitions [4]. Decades of materials science on this alloy system have yielded vast insight into niobium-uranium interactions, alloying, microstructure and process-structure-property behavior [5-27]. When rapidly quenched from the high temperature γ-BCC phase [10], U-6Nb forms a heavily-twinned, metastable α"-monoclinic phase [25]. This material possesses a shape memory response [16, 20], accommodating stress by detwinning [19, 24], followed by dislocation formation and propagation. The mechanical behavior of this material is heavily influenced by its Nb content and distribution, which determines its crystallographic structure. This microstructure is dependent upon cooling rate/thermal history and is highly process dependent. Other factors that may affect mechanical behavior include microstructure features, namely grain size [19, 28], inclusions and impurities [29], which are also influenced by the processing method [28, 30, 31].

Here, we explore laser powder bed fusion, a processing method generating substantial interest for its ability to produce near net-shape parts with high architectural complexity, of this fascinating alloy. The metals laser powder bed fusion process creates structures in a layer-wise fashion, achieving structural complexity through the use of thin layers (<100 μm), fine powder and small laser spot size [32]. Builds are often custom and the different scanning strategies, part geometries, number of builds per plate, layer size, laser parameters and material properties all contribute to complex, unique thermal conditions and solidification behavior from part to part.

The qualification of additively manufactured metals is challenged by the process variables and conditions discussed above, as well as the high degree of thermal stresses which arise during processing [33, 34] and often result in localized yielding evidenced by a high number of dislocations [35] in additively built metals. Furthermore, the welded microstructures produced via localized melting and layer-wise consolidation can result in anisotropic mechanical properties [36-38], which complicate structural simulation and design. An additional materials challenge, specific to reactive alloys such as U-6Nb, includes the potential introduction of non-metallic impurities through (1) the use of oxidized powder and (2) exposure at elevated temperatures to argon purge atmosphere impurities during building.

LLNL's investigation into laser powder bed fusion of U-6Nb is an effort spanning 2015 to present, which involves multiple powder sources with varying compositions. Two powders lots have been investigated to date. These are referred to as "Powder 1" and "Powder 2" and are described compositionally in Table 1. An effort to establish a third powder feedstock (U-6Nb powder 3) is underway. In this report, Powder 2 will be discussed only. This effort is aimed at (1) understanding the effects of laser powder bed fusion on the microstructure and mechanical behavior of U-6Nb, (2) identifying post-processing heat treatment required for homogenization and (3) determine whether it is possible and what means are necessary to achieve conventional, wrought-like mechanical behavior in laser powder bed fusion processed U-6Nb.

Element	Powder 1	Powder 2
Nb	59,600±400	60,380±950
Ti	5,340±60	4.86±0.50
Mo	2,790±30	1076±35
Zr	106±2	70.6±1.6
Ta	11.66±0.14	139±2.4
V	1.1±0.06	1936±26
W	5.93±0.11	11.1±0.18
Fe	56±5	850±21
Al	39±2	734±30
Ni	17.5±0.6	64.4±3.0
Cu	13.39±0.19	108.9±2.2
Mn	8.26±0.16	17.3±3.4
U (bal)	932,000	934,500
Wt% Nb/(U+Nb)	6.01	6.07

Table 1. Concentration of impurities in the U-6Nb powder 1 and powder 2; measurement made via ionically coupled plasma mass spectroscopy (ICP-MS). All measurements are in µg/g, unless otherwise indicated.

Section 2

Additively Manufactured U-6Nb Specimen Preparation

2.1 Precursor powder

Pre-alloyed Powder 2 particles (Fig. 1), described in detail in [39, 40], were used to process structures via laser powder bed fusion additive manufacturing. The composition of this powder, which is comprised of a broad size distribution and an oxide shell, is presented in Table 1. The powder has a mean diameter between 53 and 63 μm from sieve analysis (Fig. 2) and its microstructure and processing is described in detail elsewhere [39, 40].

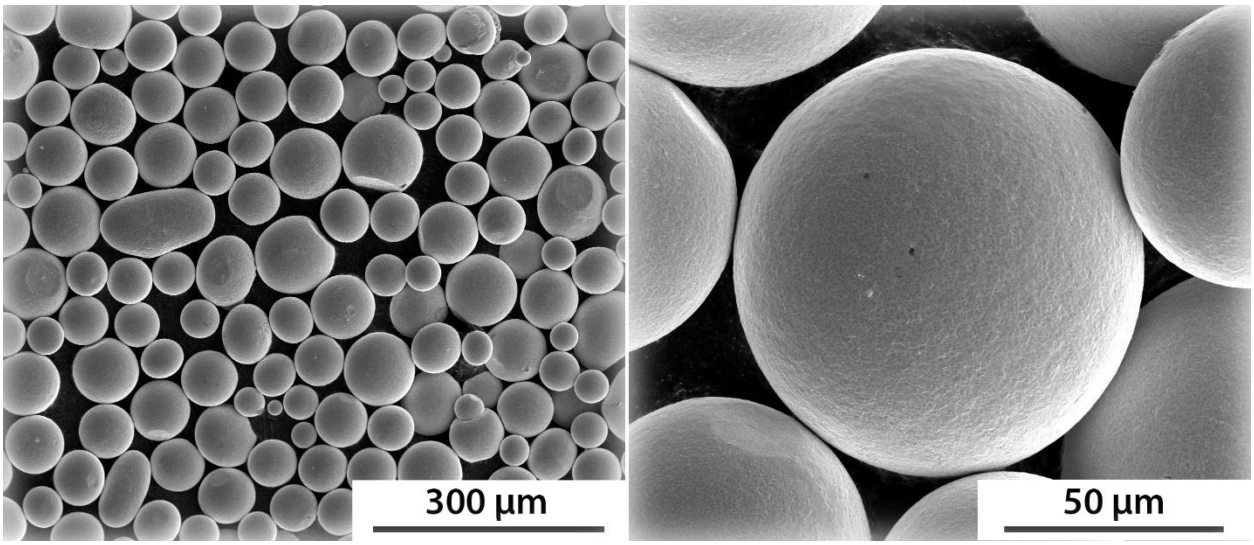

Figure 1. Scanning electron micrographs of pre-alloyed U-6Nb powder imaged at 5 keV via secondary electrons

The oxide shell, previously reported to be comprised primarily of FCC UO_2 [40], was measured on three powder particles with diameters near the distribution mean of 55 μm. Platinum was deposited on top of each particle via electron beam deposition and ion beam deposition for a final thickness of 2-3 μm to preserve the oxide for accurate thickness measurements. The oxide shell cross-section was exposed using a FEI Nova600 NanoLab dual-beam FIB equipped with a Ga+ focused ion beam and imaged using scanning electron microscopy. The oxide layer thickness at this particle size was measured between 36 and 40 nm.

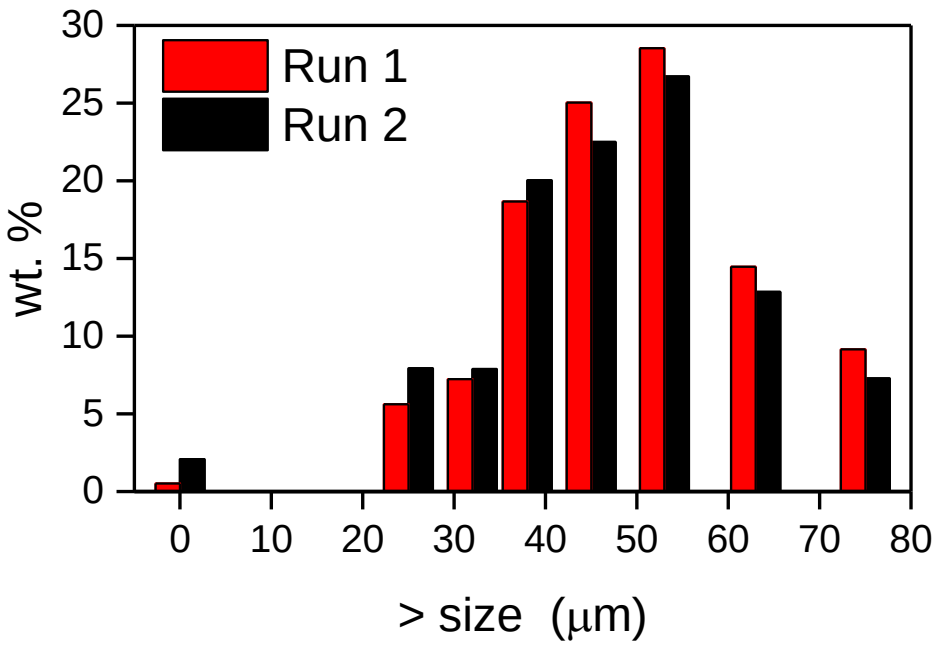

Figure 2. Particle size distribution from sieve analysis on two samplings, 200 g each, of U-6Nb powder

2.2 Laser powder bed fusion processing

The additively manufactured (AM) U-6Nb specimens were fabricated on a Concept Laser M2 powder bed system, using a 400 W Nd:YAG laser with a wavelength of 1064 nm, focused to a Gaussian beam diameter of 50 μm D4σ (where σ is the standard deviation of the intensity distribution). The beam was moved at speeds up to 1 m/s, and argon shielding gas was used to blow away the laser plume and protect the sample from excess oxidation. AM U-6Nb specimens were processed on cast U-6Nb build plates using island scanning, where the laser beam is rastered back and forth in a 5 x 5 mm square and squares are randomly deposited, yielding a checkerboard-like deposited layer with adjacent islands scanned orthogonally to each other [41]. Due to limited material quantity, all mechanical test specimens were built horizontally.

2.3 Specimen machining

Mechanical characterization specimens were removed from the build plate via wire electrical discharge machining. Cylindrical U-6Nb tensile specimens (Fig. 3) were lathe machined to a gauge length/diameter ratio of 3.2:1 due to limited material quantities—a departure from ASTM E8 [42] which requires a minimum 4:1 gage length to diameter ratio. Density measurements and microstructure analyses were performed on rectangular prism specimens (10x10x8 mm, LxWxH, 142 laser pass layers).

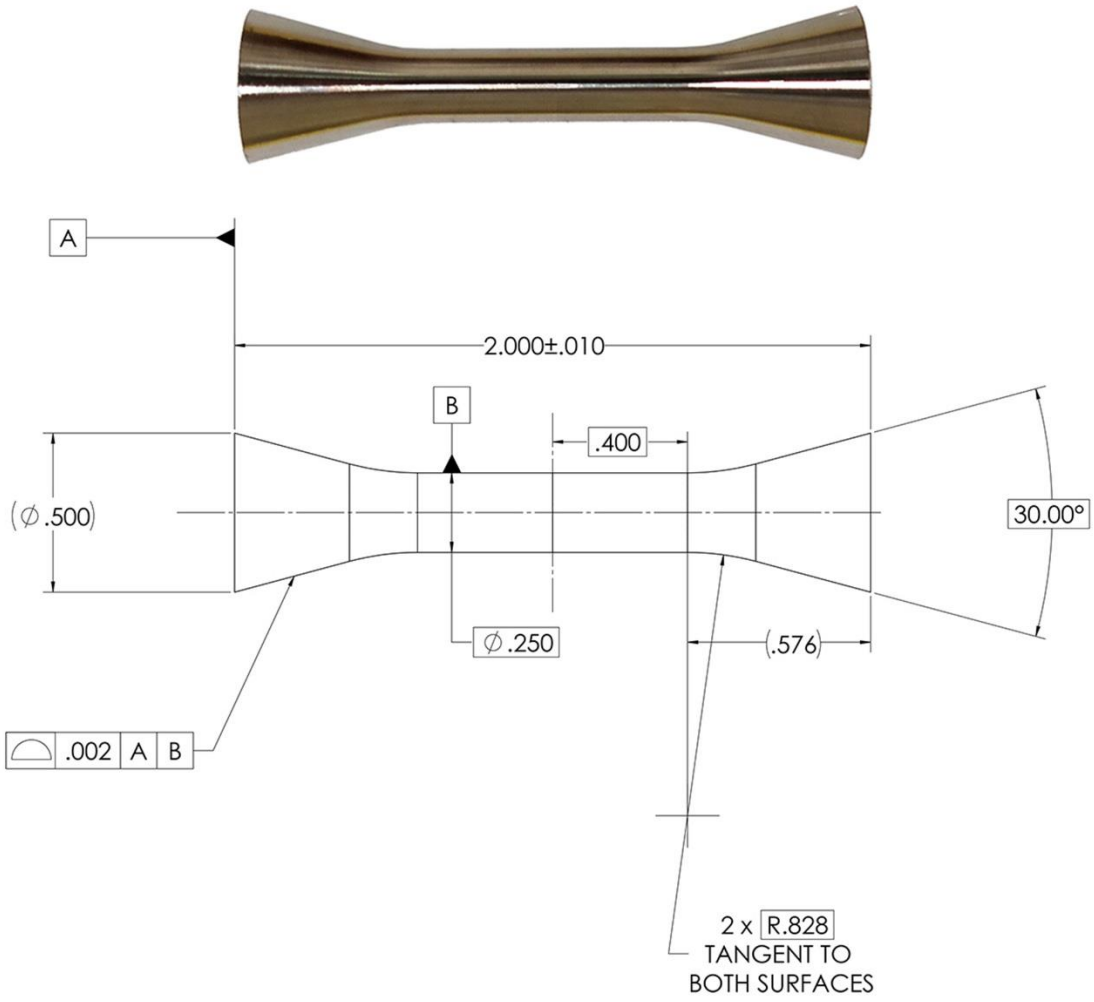

Figure 3. Tensile bar photo and schematic (dimensions provided in inches); conical ends accommodate self-alignment in the tapered grips

2.4 Solutionization and annealing heat treatments

Three post build solution annealing heat treatments (HT) were performed in a medium vacuum (6-8 mTorr) furnace on five separate tensile bars (TBs): (TB 1, AB) as built condition, (TB 2, HT 1) 840 ºC for 6 hours, (TB 3-6, HT 2) 1000 ºC for 16 hours, followed by cooling to 840 ºC and a 30-minute hold at 840 ºC. All post build heat treatments were followed with an immediate water quench (WQ) to form the monoclinic phase. Specimens exhibited minimal geometrical distortion upon post build HT.

Measurements during *in situ* annealing using the Spectrometer for Materials Research at Temperature and Stress (SMARTS) diffractometer at the Manuel Lujan Jr. Neutron Scattering Center, LANSCE, Los Alamos National Laboratory showed no change in lattice constants while under (HT 3) isothermal soak after heating from room temperature to 1000ºC (Fig. 4). This lack of change indicates that the AM U-6Nb specimen is homogenized during the heating (approximately 1 hour) from room temperature to 1000ºC. This timescale for homogenization is reasonable, given the typical solidification cell spacing of 0.7-2 µm in AM U-6Nb specimens (see Section 5) and the niobium diffusion rates in uranium (Fig. 5).

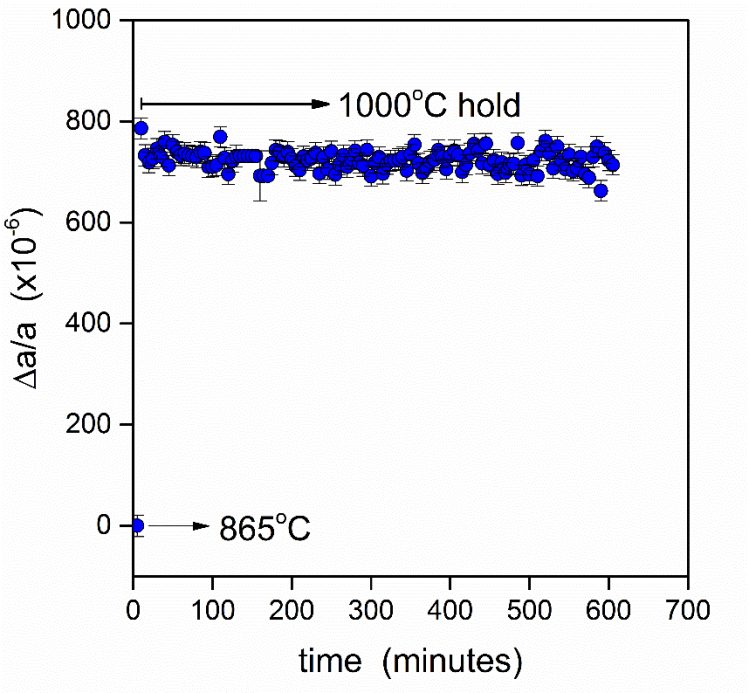

Figure 4. Lattice constant evolution during a 1000°C hold measured via in situ neutron diffraction

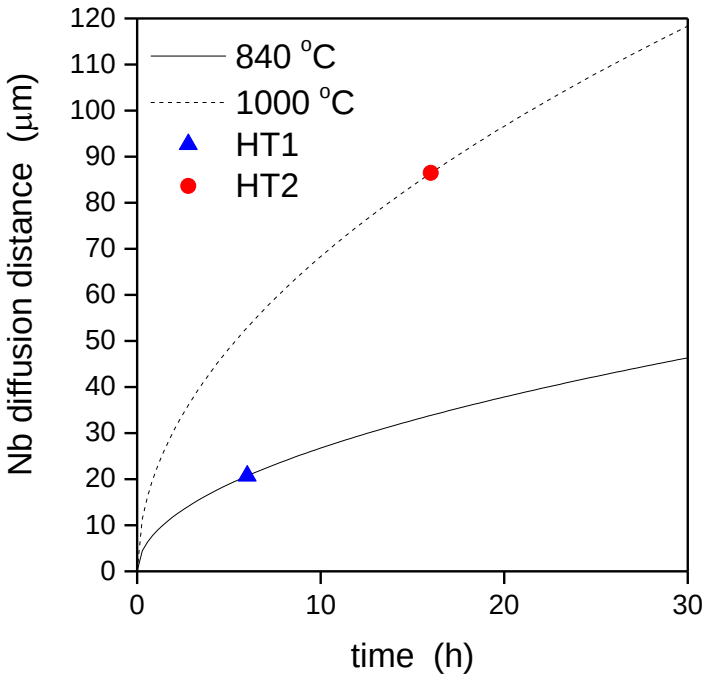

Figure 5. Niobium diffusion distance in uranium, plotted at 840°C and 1000°C, with selected heat treatments indicated in blue and orange, determined using D_0=1.5 (10^{-4}) cm^2/s and Q=33 kcal/mol [5, 43]

Section 3

Composition and Crystallography

3.1 Bulk metallic composition

Compositional analysis (Table 2) was performed using inductively coupled plasma mass spectrometry (ICP-MS). The nonmetallic impurities (carbon and oxygen) were measured using inert gas fusion (IGF) and are discussed in more detail in Section 4. It must be noted that this powder batch does not meet standard wrought U-6Nb specifications, therefore these AM builds will not, as no refinement occurs during the laser powder bed fusion process.

Table 2. Concentration of impurities in the U-6Nb powder and U-6Nb specimens after powder bed fusion processing measured via ICP-MS. All compositions are in µg/g unless otherwise noted.

Element	Wrought specification	Powder 2	As built
Nb		60,380±950	60,100±120
V		1,936±26	1,913±44
Mo		1,076±35	1,105±14
Al	<75	734±30	806±43
Fe	<150	850±21	903±48
Ta	<2,500	139±2.4	142±1.7
Cu	<100	108.9±2.2	102±4.2
Zr	<500	70.6±1.6	88.0±1.4
Ni	<75	64.4±3.0	76.5±2.6
W		11.1±0.18	11.8±0.17
Ti	<75	4.86±0.50	5.82±0.54
Mn		17.3±3.4	17.8±0.59
O		300 (from supplier)	430±28
C	<200	855±3	1,100±100
U (bal)		934,500	934,600
Wt% Nb/(U+Nb)	5.2 wt% < Nb < 6.5 wt%	6.07	6.04

3.2 Effect of AM on metallic composition

In any process involving localized thermal spikes, concerns regarding material vaporization are not unfounded. Vaporization is known to occur during the laser powder bed fusion process, as evidenced by keyhole-shaped welds or melt pools [44, 45]. In an alloy system, with components of different melting and boiling points, it is possible that laser powder bed fusion processing will result in a different composition. For example, in the alloy Ti-6Al-4V, aluminum is known to be unintentionally removed during laser powder bed fusion [46]. This occurs due to (1) temperatures required to boil the aluminum and (2) air flow across in the laser powder bed fusion chamber. Note that the air flow is a necessary

aspect of the laser powder bed fusion process—laser energy is drastically reduced as it travels through a metal vapor plume, resulting in insufficient melting of the powder bed and lack of fusion voids in builds.

Despite these concerns, which affect other alloy systems, the uranium and niobium composition appears unaffected by the laser powder bed fusion process (Fig. 6). The powder used for this particular analysis is of a different pedigree than that used in the rest of this study; however, these results remain valid. These results imply that any uranium vapor produced during the AM process is deposited locally, onto the build surface. Observations by the operators—that there is substantially less of a visible vapor plume in the U-6Nb alloy during laser powder bed fusion—provide support that the processing parameters selected do not result in substantial uranium vaporization.

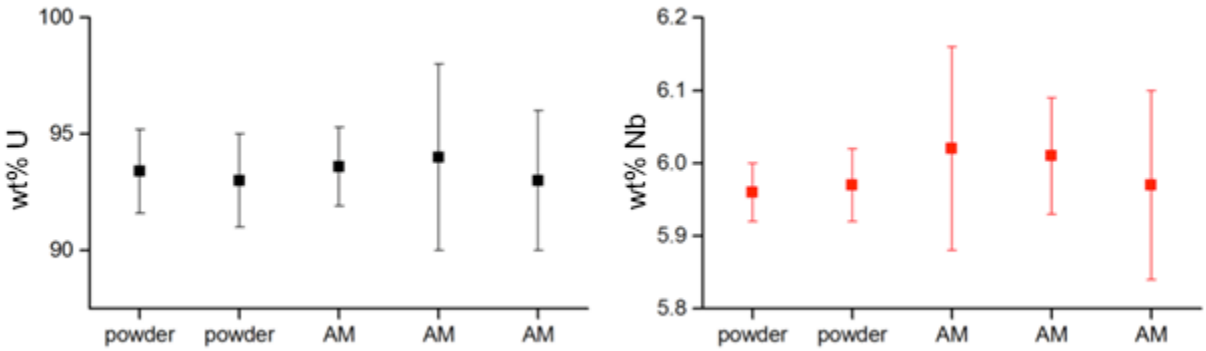

Figure 6. Uranium and niobium detected in two powder samples and three randomly selected AM samples, measurements via ICP-MS.

3.3 Crystallography

Neutron diffraction was performed on the Spectrometer for Materials Research at Temperature and Stress (SMARTS) diffractometer at the Manuel Lujan Jr. Neutron Scattering Center, LANSCE, Los Alamos National Laboratory. Details of the neutron diffraction facility and analysis are discussed elsewhere [47].

Neutron diffraction was used to measure phase fractions in the AM parts with a 2 mm^3 interaction volume, which is considered to represent a statistical average over a large number of grains. Diffraction patterns were analyzed for phase fractions using a Rietveld analysis [48] on the starting powders, the as-built samples, and the post heat treated samples. Rietveld analysis was completed on the diffraction data using the General Structural Analysis System (GSAS) software package developed at Los Alamos [49]. For the α'' structure, the space group used in the analysis was (C 1 1 2_1/m) with 2 equivalent atom positions, (x, y, z) and (-x,-y, z + ½), each with a multiplicity of 4. The non-conventional space group facilitated comparison of the low Nb concentration orthorhombic phase with the monoclinic phase at intermediate Nb concentrations, with the transformation being manifested by the deviation of the angle between the a and b lattice vectors from 90° [11]. For the γ^0 structure a P4/nmm space group was used.

Neutron diffraction patterns are presented in Fig. 7 for the alloy in the different conditions, including the feedstock powder. Analysis of these diffraction peaks was performed to calculate the fraction γ^o and α'' for each condition. Note that the feedstock powder and AM build each possess both α" and γ^0 phases. An example of the nearly 100% α'' diffraction pattern is shown in Fig. 7c, after the AM build has been homogenized and water quenched.

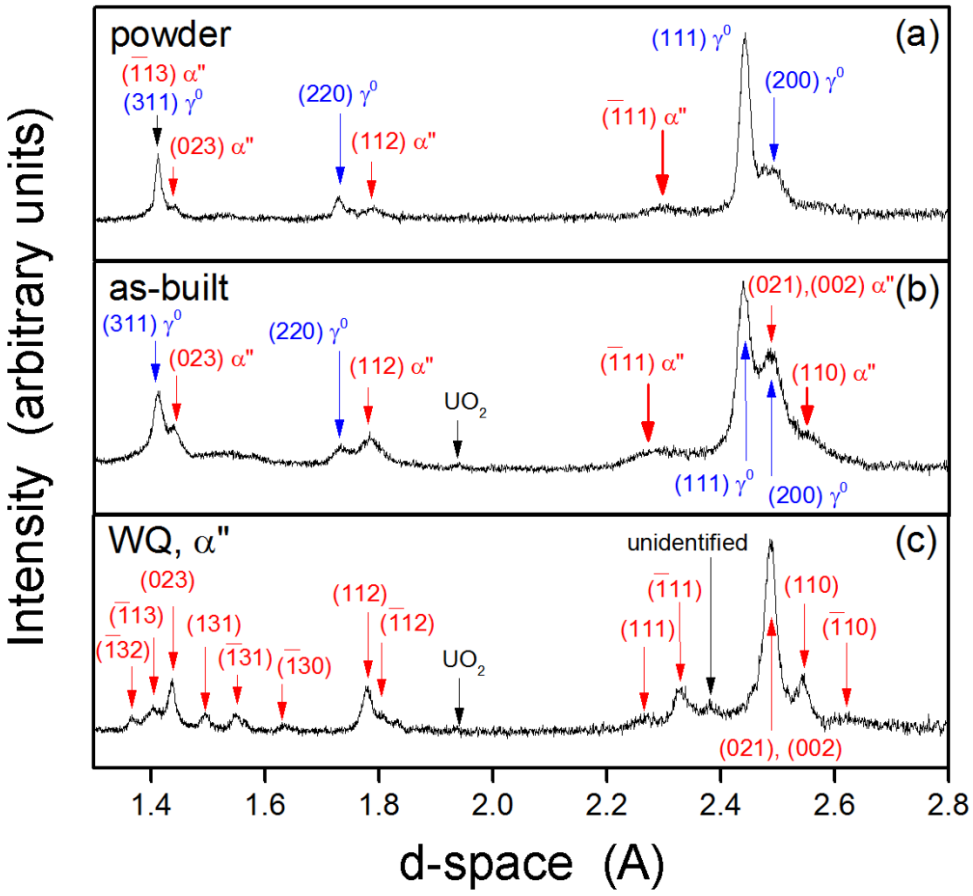

Figure 7. Diffraction patterns from U-6Nb for the Powder 2 material (described in Table 1 and 2) in: a) powder, b) as-built, and c) homogenized/WQ condition

Section 4

Oxidation and Nonmetallic Impurities

4.1 Impurity content

Inert gas fusion (IGF) analysis was used to analyze the nonmetallic impurity content in four specimens (Fig. 8). These specimens consist of two U-6Nb "standard" wrought specimens produced via vacuum induction melting and vacuum arc remelting cycles (VVV) acquired from tensile bar ends, one powder sampleand one laser powder bed fusion processed sample. IGF was performed at the Y-12 National Security Complex Plant Lab using LECO ONH and LECO CS analyzers [50]. Missing data (carbon and hydrogen for VVV samples and oxygen and hydrogen for the powder samples) in Fig. 8 is due to lack of instrument availability and not representative of a zero quantity measurement. Lower detection limit for a 1 g sample is 0.05 µg/g oxygen, 0.05 µg/g nitrogen, 0.1 µg/g hydrogen and 0.6 µg/g carbon.

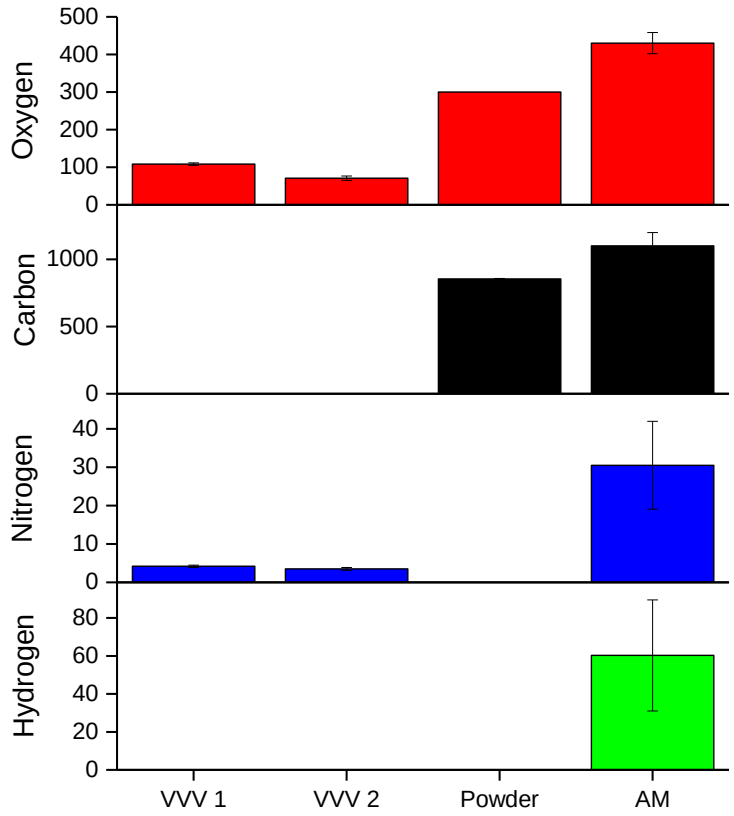

Figure 8. Nonmetallic impurity content in µg/g measured using IGF; note that the oxygen values shown in the powder specimens were provided by the powder manufacturer.

Oxidation which occurs during the laser powder bed fusion process will be affected by the chamber atmosphere (which is in turn influenced by the purge gas flow rate, chamber design and seals, argon purity, etc.) and the build thermal conditions (laser settings and scanning strategy). The average oxygen in three as-built specimens was measured using inert gas fusion analysis [50] and is reported as 430±28 ppm. Presently, the amount of oxidation/gettering that occurs during the laser powder bed fusion process relative to the oxygen content due to powder surface oxidation is unknown. The manufacturer specifications for oxygen content in the powder samples is reported at 300 ppm (Fig. 8); however, their analysis method and uncertainty were not provided.

We have addressed this issue in another reactive alloy, Ti-6Al-4V, with a starting powder oxygen content of 0.17 wt% as measured via IGF. In the Concept Laser M2 chamber used to process the Ti-6Al-4V and the U-6Nb specimens, an oxygen uptake ranging from none to 0.08 wt% (Fig. 9) was observed in builds A-F, 10.2 cm (4 in) tall, 1.3 cm (0.5 in) diameter [51]. The oxygen content varies from 0.16 to 0.25 wt.% at various specimen locations and heights. The only discernable pattern is observed in pillar F, which was located downstream of the rest of the builds. This is attributed to contamination from the vapor plume, which swept from A to F.

Note that there is a rigorous cleaning procedure during transitions between Ti-6Al-4V and U-6Nb builds and, as a result, no Ti impurity uptake was observed in the U-6Nb builds and no radioactive material was present in the Ti-6Al-4V builds.

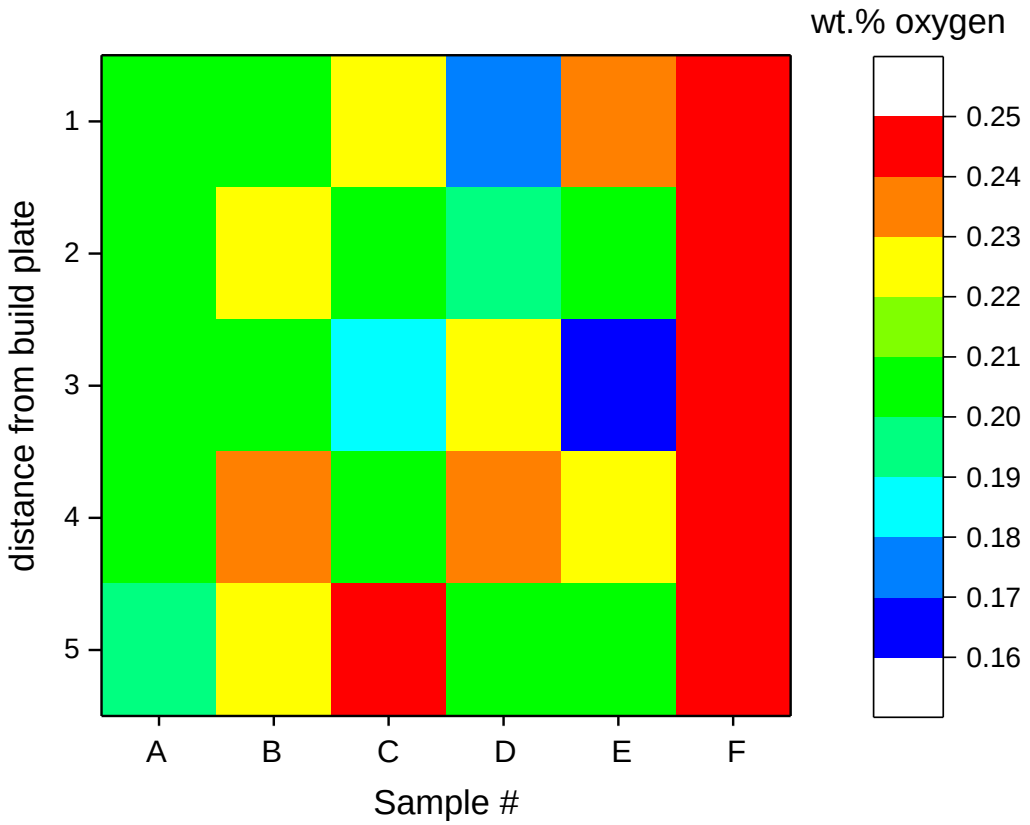

Figure 9. Oxygen level in each Ti-6Al-4V specimen built using the Concept Laser M2 [51]

4.2 Impurity form

Note from Fig. 8 that the oxygen and nitrogen impurity levels are higher than those detected in conventional, wrought processed U-6Nb. Based on prior dehydriding investigations, hydrogen may be removed during the post-processing vacuum anneal; however, data to support this has not yet been produced. There has been some investigation into the behavior of oxygen in AM U-6Nb material, which will be discussed in this section.

Recall that the chemical composition of the powder shell oxide (as FCC UO_2) was verified via selected area diffraction [40]. The presence of UO_2 in the pre-alloyed powder is noteworthy, considering that its high melting point (2865 °C) will promote its retention in any powder bed fusion builds. Evidence of oxidation during the build process is noted in the darkening of each newly created melt pool surface, as observed through the build chamber window.

Also, neutron diffraction spectra, acquired using the SMARTS diffractometer at the Lujan Center in Los Alamos, of the powder and AM builds shows a resolvable UO_2 peak in the as built specimen (Fig. 10, red curve), compared with the powder samples (green and purple curves)—these three curves were acquired using the same count time. The lack of resolvable peak in the powder specimens may represent an inability to resolve UO_2 present at 10^1 nm size scales (i.e., powder oxidation layer). At a higher count time, this peak (black curve) sharpens after post build HT (blue curve), consistent with a report by Hsiung et al. that the UO_2 inclusions increase in size from 20 nm in as built specimens (Fig. 11) to 200 nm in specimens HT for 6 hours at 1000ºC.

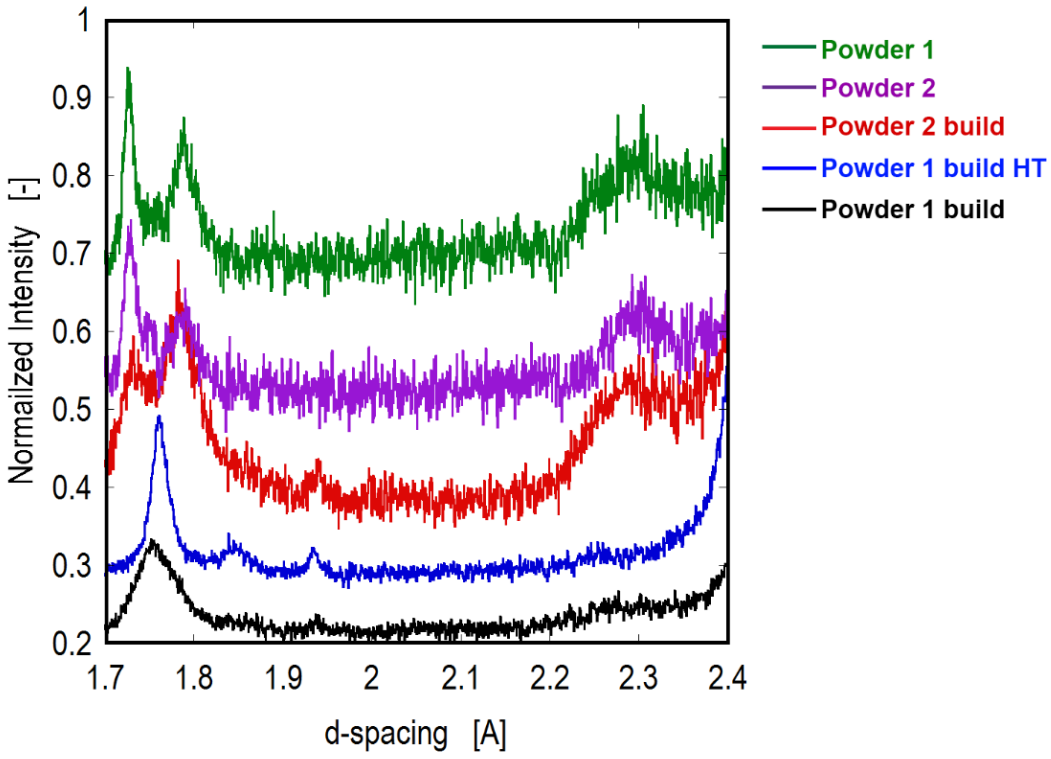

Figure 10. Neutron diffraction spectra of two powder samples, builds and one HT build, acquired via SMARTS diffractometer

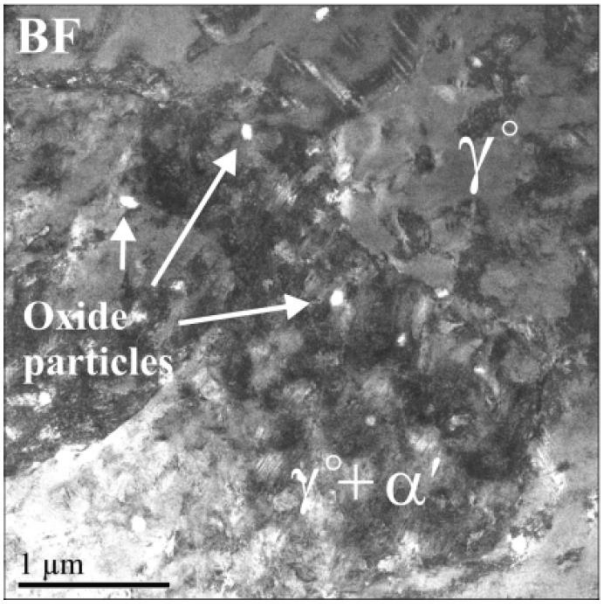

Figure 11. Oxide particles observed in an AM build via transmission electron microscopy [52]

Section 5

Microstructure

U-6Nb specimens were sectioned, potted, polished using traditional metallography techniques. Specimens were final polished used 5 wt.% chromium trioxide (CrO_3) in H_2O in a vibratory polisher for polarized light microscopy. This was followed with an electrolytic etch using 1 part ortho-phosphoric acid (H_3PO_4) and 1 part H_20 (1-5 V, open circuit, stainless steel cathode and anode) to reveal grain boundaries and inclusions.

5.1 As built microstructure

The as built U-6Nb microstructure is traceable to its welded origins, with darker regions of the optical image in Fig. 12 and 13 indicating the partially melted zone of each laser pass. Laser scan lines are rotated 90° with each layer and melt pools in the range of 190 µm deep are formed. Small sized porosity is evident (relative part density is 99.5%) and there are no noticeable inclusions observable at this scale.

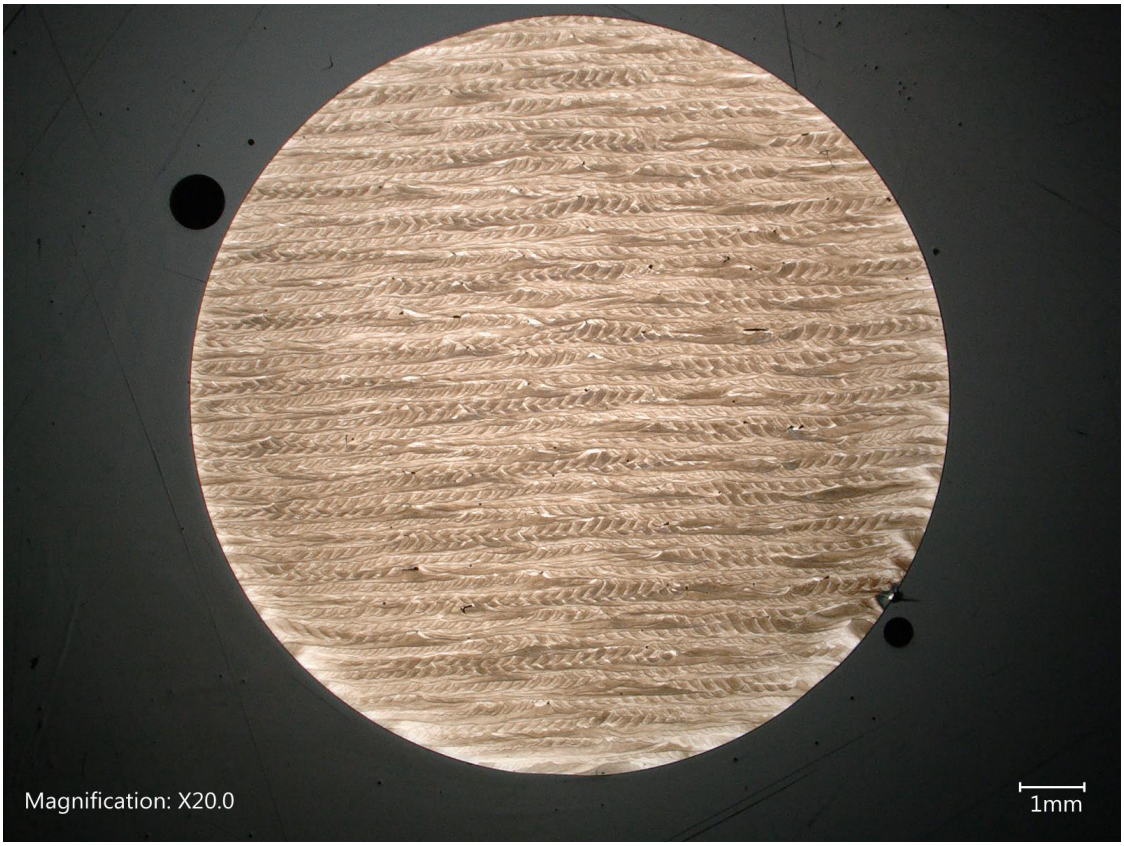

Figure 12. Melt pool structure observed at a 45° cross-section of an as built AM U-6Nb specimen imaged via optical microscopy

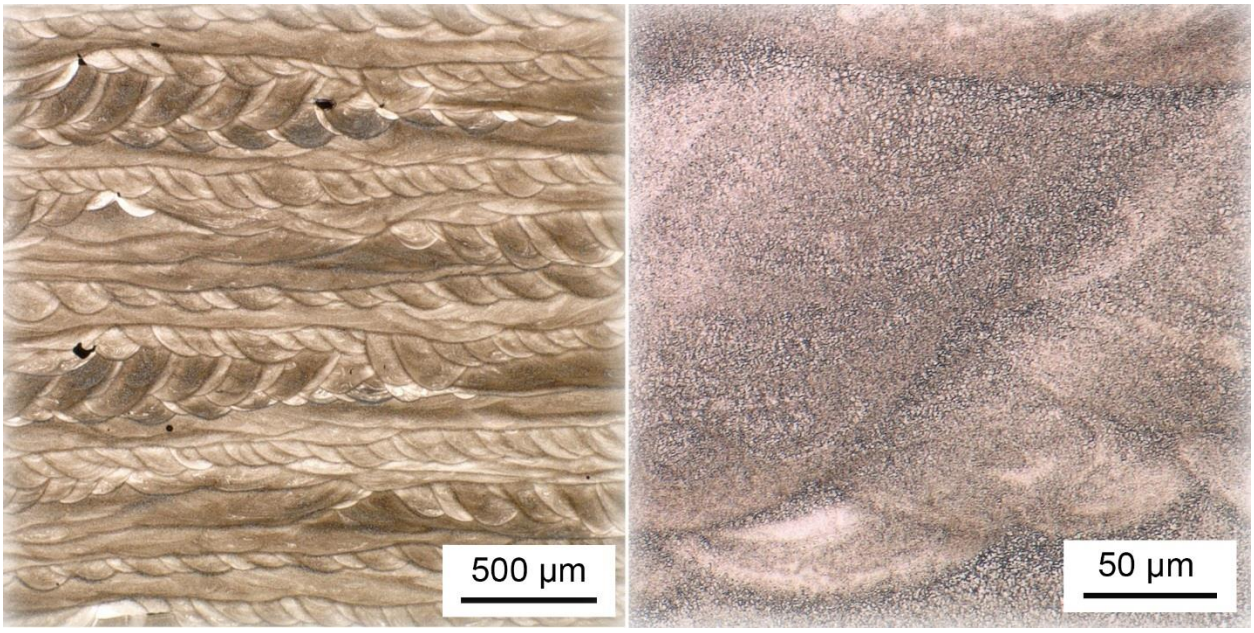

Figure 13. Higher magnification images depicting the melt pool structure observed at a 45° cross-section of an as built AM U-6Nb specimen imaged via optical microscopy

Solidification microstructure with a cell spacing of ~0.7 µm is depicted in Fig. 14; the region shown is far from the partially melted zone, located near the center of the melt pool.

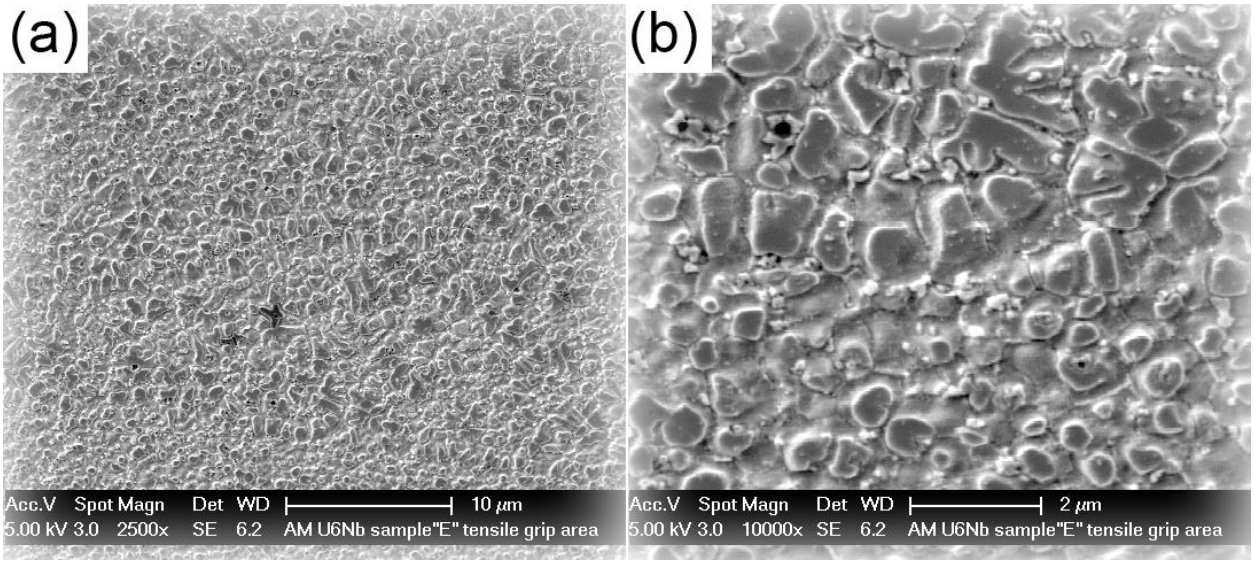

Figure 14. Solidification cells observed at a 45° cross-section in an as built AM U-6Nb specimen imaged via scanning electron microscopy at 5 kV (a) lower and (b) higher magnification

5.2 Effect of post build heat treatment on microstructure

5.2.1 Grain size

Recrystallization occurs upon heating to 1000ºC, as shown in Fig. 15. The AM U-6Nb grains are comparable in size to wrought U-6Nb (<50 µm), after a 16 hour heat treatment (Fig. 15b). Note that these grains imaged in Fig. 15 are prior γ grains that existed at elevated temperature during the anneal. After the water quench, they have martensitically transformed to the α" phase, with a twin structure consisting of finely twinned laths or bands. The twinned laths or bands (transgranular twins on the order of 10 µm) and the fine intraband twins (sub nm twins) are typically observed in martensitically-formed α"-monoclinic U-6Nb and are described in detail in [53]; these are shown imaged using transmission electron microscopy (Fig. 16).

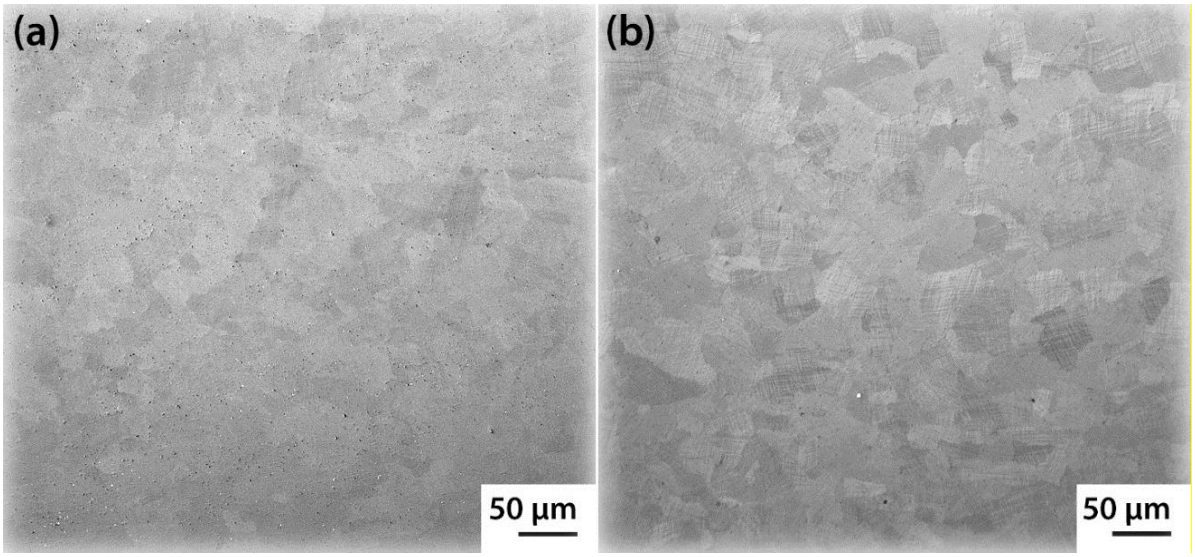

Figure 15. Microstructure of AM U-6Nb specimens annealed at (a) 840ºC for 6h and WQ and (b) 1000ºC for 16h, followed by a 30 min hold at 840ºC and WQ. Optical images of polished and etched surfaces.

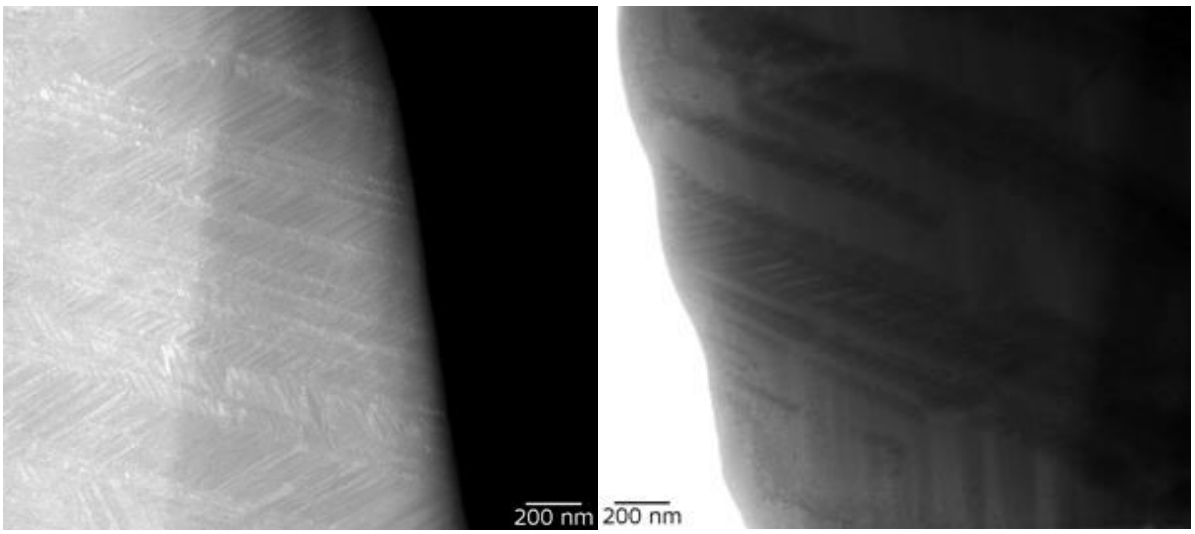

Figure 16. Transmission electron micrographs depicting finely twinned laths or bands. High-angle annular dark field scanning TEM (left) and conventional bright field imaging (right).

5.2.2 Inclusions

Inclusions are present within grains and at grain boundaries in specimens annealed at 1000ºC for 16h, followed by a 30 min hold at 840ºC and WQ. Many of the inclusions in Fig. 17 manifest at grain boundaries, lending evidence in favor of coarsening during the long post build heat treatment. The typical size is <10 µm.

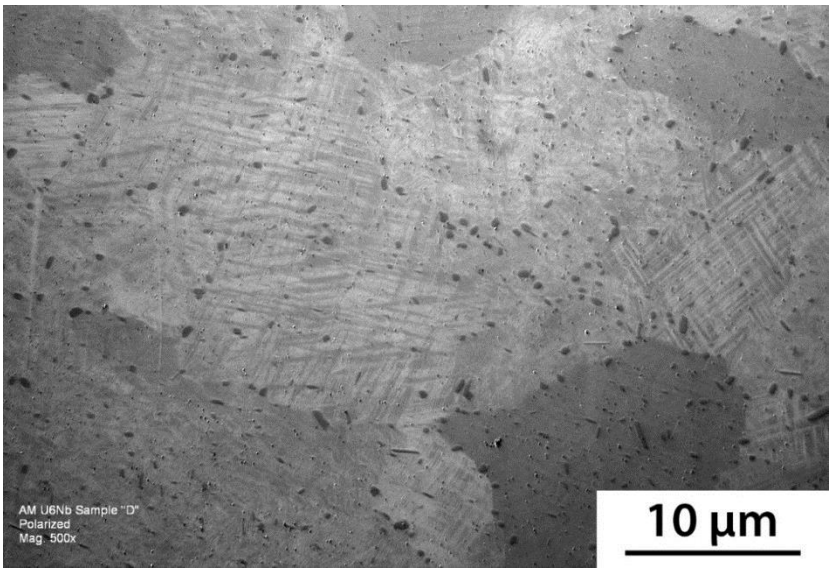

Figure 17. Optical micrograph of an AM U-6Nb specimens annealed at 1000ºC for 16h, followed by a 30 min hold at 840ºC and WQ

At higher magnification, there appears to be two different morphologies present: rod-like and round (Fig. 18). Energy dispersive X-ray spectroscopy (EDS) was performed on three different regions (Fig. 19). These results are summarized in Table 3.

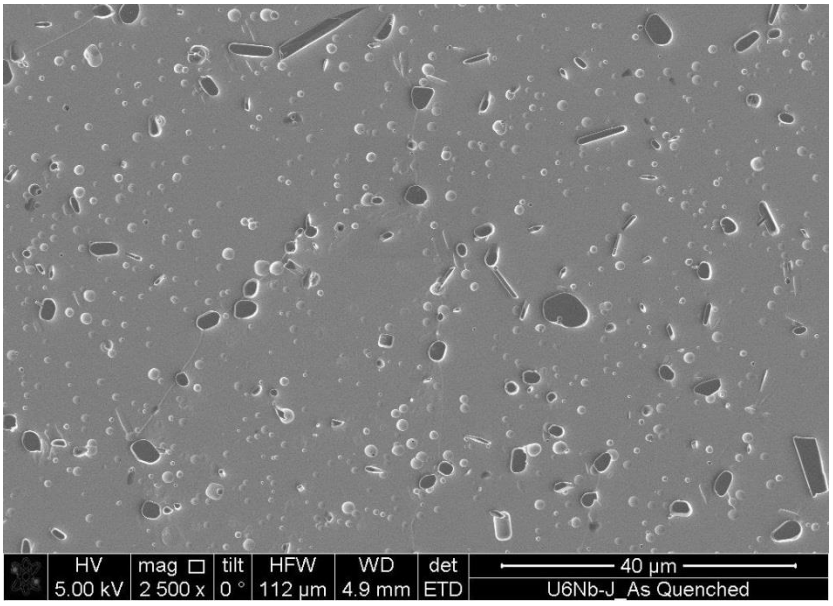

Figure 18. Scanning electron micrographs of an AM U-6Nb specimen annealed at 1000°C for 16h, followed by a 30 min hold at 840°C and WQ, imaged at 5 keV via secondary electrons

The rod-like inclusion is comprised of Nb, Si and Al, while the round inclusion is comprised of Nb. The rod-like and round particles were each sectioned via ion milling to reveal their 3D morphology (Fig. 20). We conclude that the highly elongated, faceted inclusions are rod-like and the round inclusions are equiaxed. These inclusions vary in morphology and composition from conventional wrought inclusions, which include UO_2 (globular), Nb_2C/NbC/UC (sharp angular faces) [5].

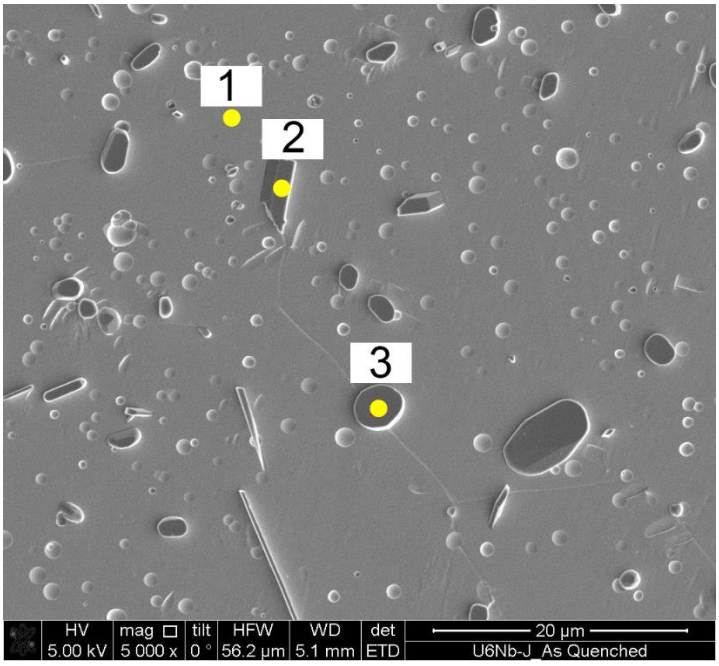

Figure 19. Scanning electron micrographs depicting EDS regions on an AM U-6Nb specimen annealed at 1000°C for 16h, followed by a 30 min hold at 840°C and WQ, imaged at 5 keV via secondary electrons

Table 3. Composition measured via uncalibrated EDS in at% for regions 1-3, specified in Fig. 18

	Region 1	Region 2	Region 3
U	36.0	1.7	0.5
Nb	4.7	45.7	52.0
C	37.2	18.3	37.9
O	22.1	9.5	8.7
Al	--	7.3	0.2
Si	--	17.5	0.9
Shape	Matrix	Rod-like	Round/equiaxed

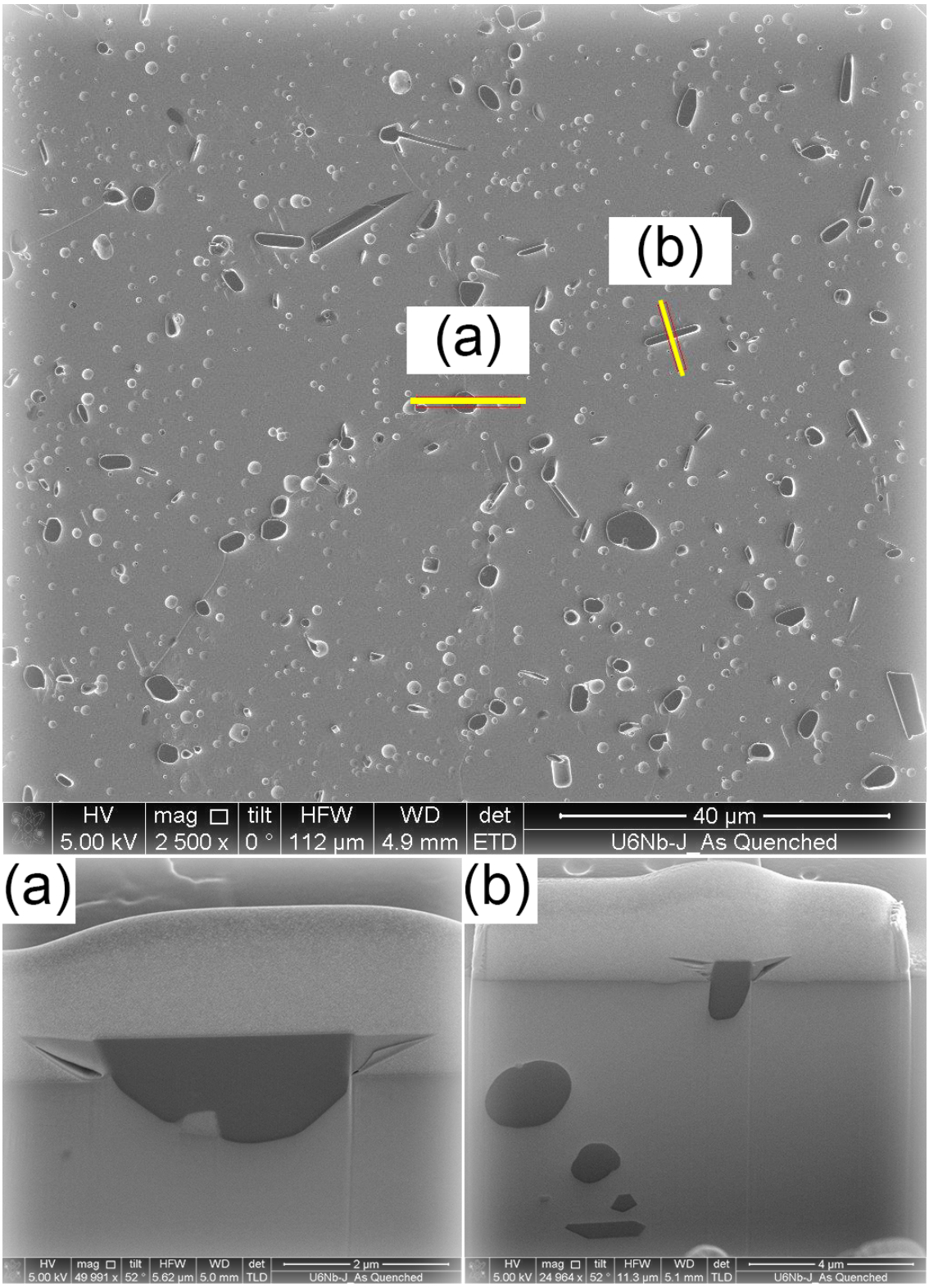

Figure 20. Scanning electron micrographs depicting inclusions and their cross-sections observed in an AM U-6Nb specimen annealed at 1000ºC for 16h, followed by a 30 min hold at 840ºC and WQ, imaged at 5 keV via secondary electrons. (a) Image showing section locations, (b) cross-section 1, (c) cross-section 2

It should be noted that the rod-like and round/equiaxed inclusions appear to coarsen with time and temperature during post build heat treatment (Fig. 21). Circular indentations apparent on the surface of these polished and etched U-6Nb builds are likely etch pits.

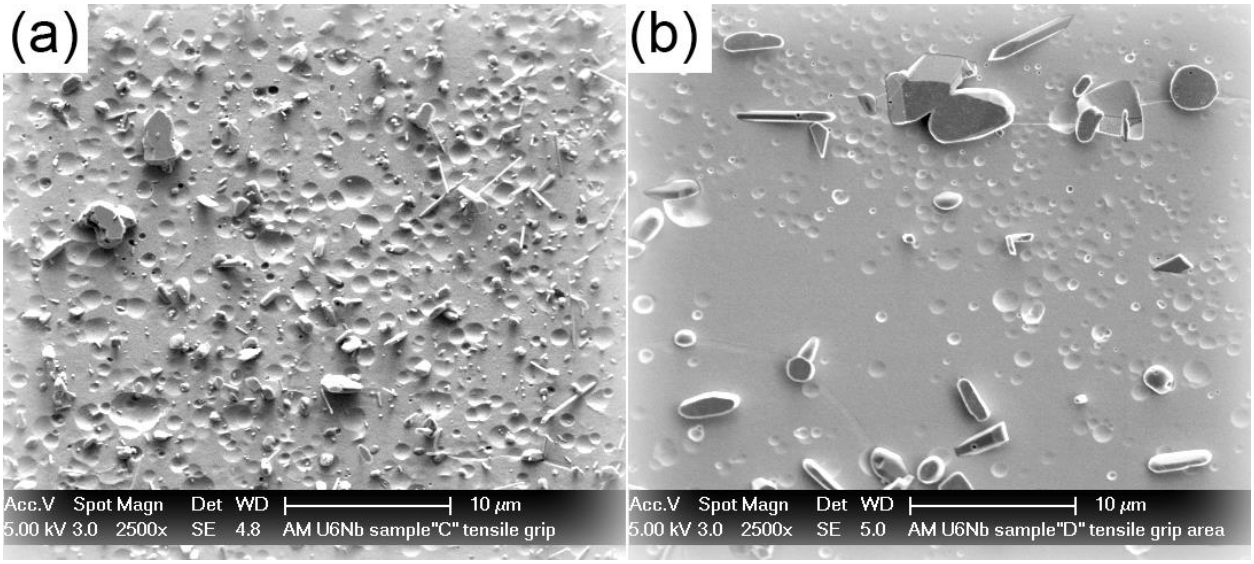

Figure 21. Inclusions shown in (a) an AM HT1 build and (b) an AM HT2 build, imaged at 5 keV via secondary electrons

The presence of Nb, Si and Al is confirmed via EDS in the TEM chamber. Small amounts of V are also detected within the faceted, rod-like inclusions (Fig. 22). EDS mapping reveals other impurities present in the rod-like inclusions (Fig. 23). The Si and Al impurities appear to be distributed across the rod-like inclusions (Table 4). In fact, intermetallic compounds comprised of Nb-Si-Al are reported in the literature [54].

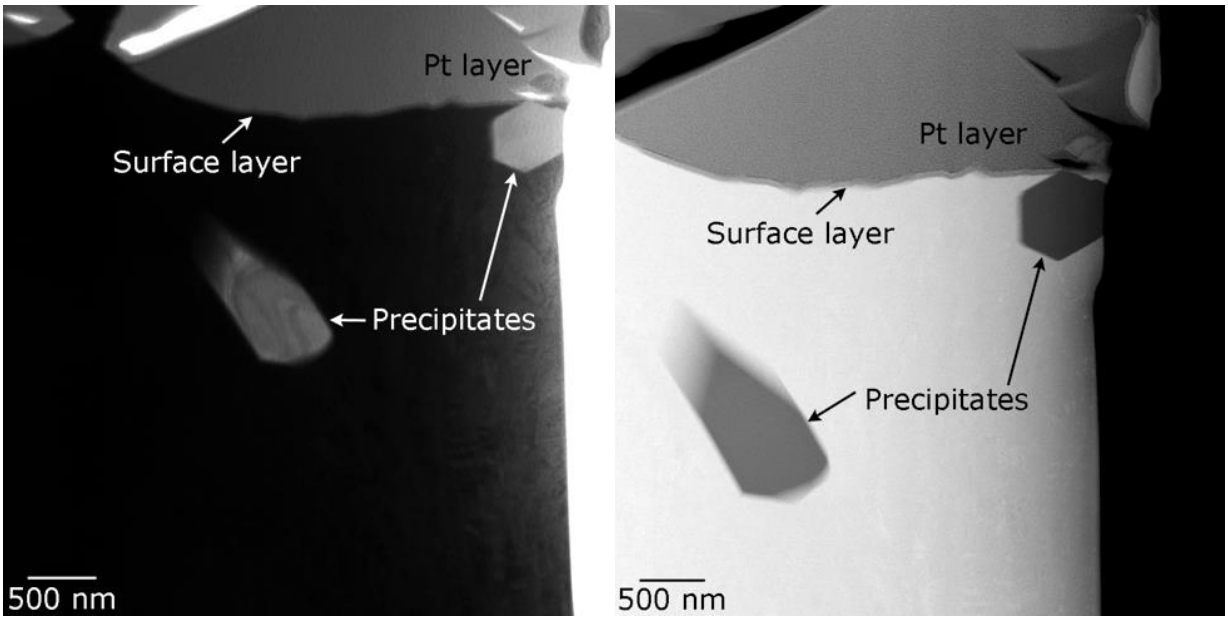

Figure 22. Inclusions present in an AM build after annealing at 1000°C for 16h, followed by a 30 min hold at 840°C and WQ

Table 4. Composition in a rod-like inclusion measured via EDS in the TEM chamber, shown in at%.

	Region 1
Nb	55.2
Si	25.3
Al	15.7
V	3.8

EDS composition of the round inclusions (Table 4) provides evidence that these are comprised of Nb carbide; however, Nb carbides are known for their faceted, irregular surfaces [5]. Note that, in Fig. 23, a stronger hue indicates a higher concentration in a region.

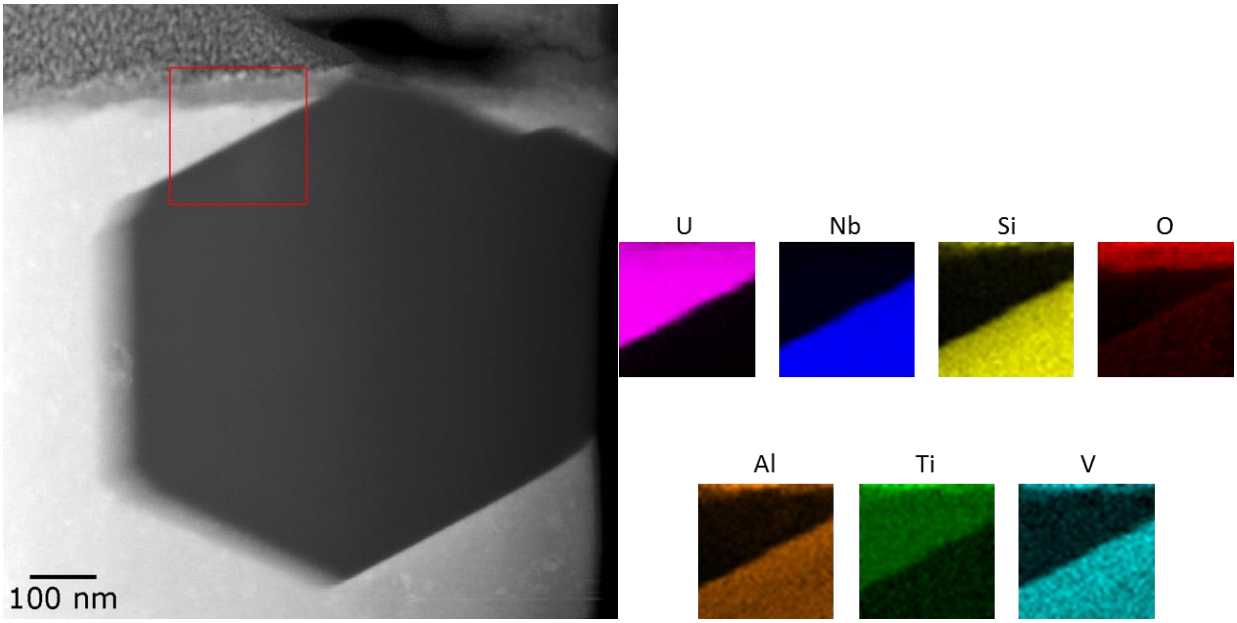

Figure 23. EDS mapping acquired in the TEM chamber across the rod-like precipitate, matrix and surface layer

Section 6

Mechanical Behavior and Failure Analysis

6.1 Quasi-static tensile testing

Mechanical performance under tensile deformation was evaluated at room temperature with a loading rate of 0.01 mm/s, corresponding to a strain rate of order 10^{-4} s^{-1}, using an Instron 4400R universal testing machine with a custom fixture and strain gage extensometer, 12.48 mm (0.49 in) long, for strain measurement. All specimens were tested to failure in the as-annealed condition (i.e., builds were machined prior to annealing).

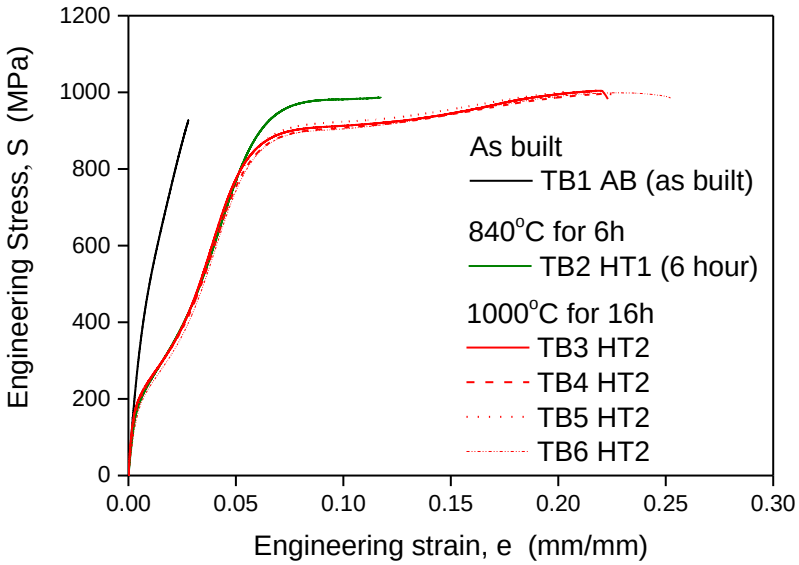

Figure 24. Quasi-static tensile engineering stress-strain behavior of AM U-6Nb specimens annealed at different time/temperatures.

After solutionization for 16 hours, a significant increase in failure strain (from 2.8% strain in the as built condition, to 11.7% strain in the 840ºC 6h HT1 WQ condition, to 22.3% strain in the 1000ºC 16h HT2 WQ condition) is observed (Fig. 24). Note that the as built TB1 failed outside the extensometer gage length. All other tensile specimens tested failed within the extensometer gage section. Prior investigations reveal two effects of annealing on microstructure: grain growth and inclusion coarsening [52]. Both phenomena can explain the difference in failure strain and second yield stress (2YS). Grain growth can reduce yield stress in many metals [55-57]; however, this is demonstrated to have little to no effect in U-6Nb [31]. Inclusion coarsening, coupled with grain boundary migration can reduce microvoid initiation sites, potentially postponing catastrophic failure.

A comparison between the quasi-static tensile behavior of AM U-6Nb and wrought processed U-6Nb is made in Fig. 25. The AM U-6Nb possesses higher yield stresses (1YS—initial yielding due to detwinning [24] and 2YS—second yielding due primarily to dislocation behavior), possibly as a result of a larger quantity of inclusions. Efforts to better quantify this are underway. The failure strain of the 16h HT and WQ AM U-6Nb is comparable to the WQ wrought specimen failure strain.

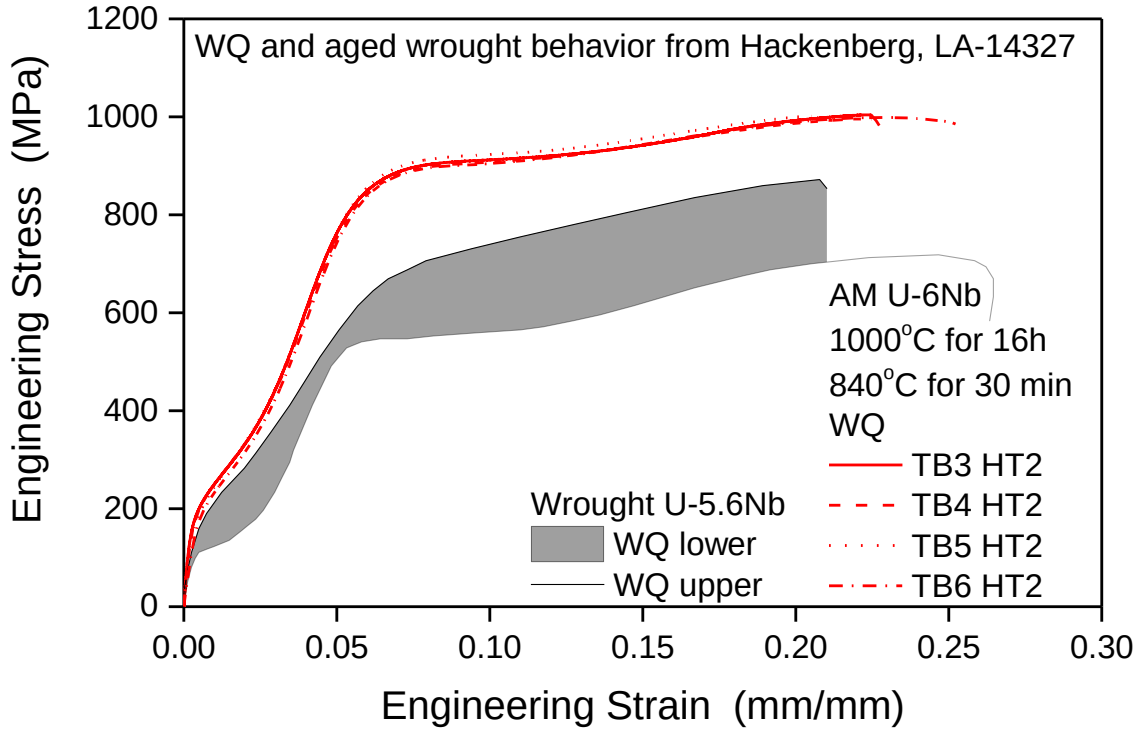

Figure 25. Quasi-static tensile response of AM U-6Nb, shown in comparison with wrought processed U-6Nb [58]

6.2 Deformation behavior

Specimens experience a slight, but measurable reduction in cross-sectional area (%RA) with post build heat treatment (TB2=2.35, TB3=7.35), as shown in Fig. 26. Recall that Fig. 26a (TB1) failed just outside the gage section, so no RA analysis is possible.

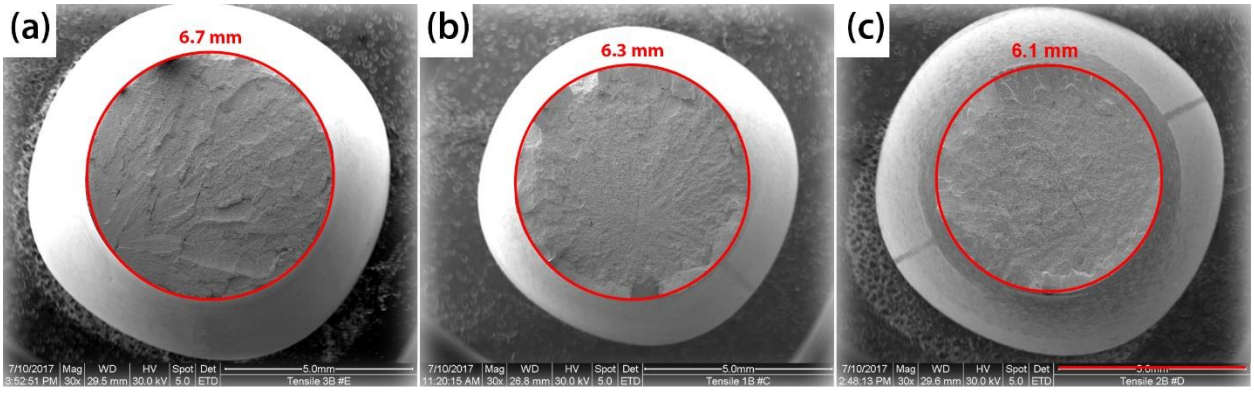

Figure 26. Fracture surface of (a) AM TB1 in the as built condition, (b) AM TB2 in the 840°C 6h HT WQ condition and (c) AM TB3 in the 1000°C 16h HT WQ condition acquired using scanning electron microscopy, E-SEM, 30 kV

6.3 Failure analysis

The as built specimen exhibits low ductility, with very little shear lipping (Fig. 27). The post build heat treated specimens exhibit ductile behavior with no brittle cleavage, evidenced by ductile dimpling (Fig. 27-29) and shear lip formation (Fig. 26, 28, 29). Failure is defect driven at multiple scales, with macrovoid initiation at process induced irregularities (Fig. 27-30) and microvoid formation at brittle inclusions (Fig. 31-32). In Fig. 28-30, an unmelted particle is observed at the fracture surface. This is not an atypical observation at a tensile failure surface and it is reasonable that such a site would act as a failure initiation point. Note also that the dimples in Fig. 30 appear faceted, with a high deviation in surface topology at scales larger than the dimples. Dimples appear to be <1 μm in the AB specimen, 1-4 μm in the HT1 specimen and ~10 μm in the HT2 specimen (Fig. 30-32).

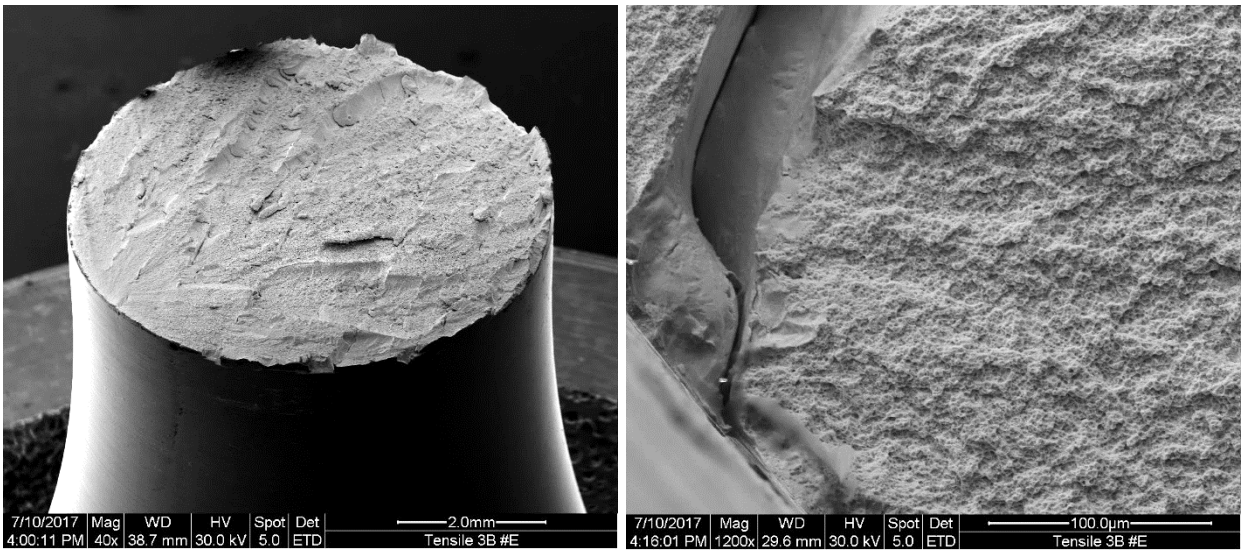

Figure 27. Electron micrographs acquired via E-SEM, 30 kV, of the failure surface of an AM U-6Nb specimen tested in the AB condition

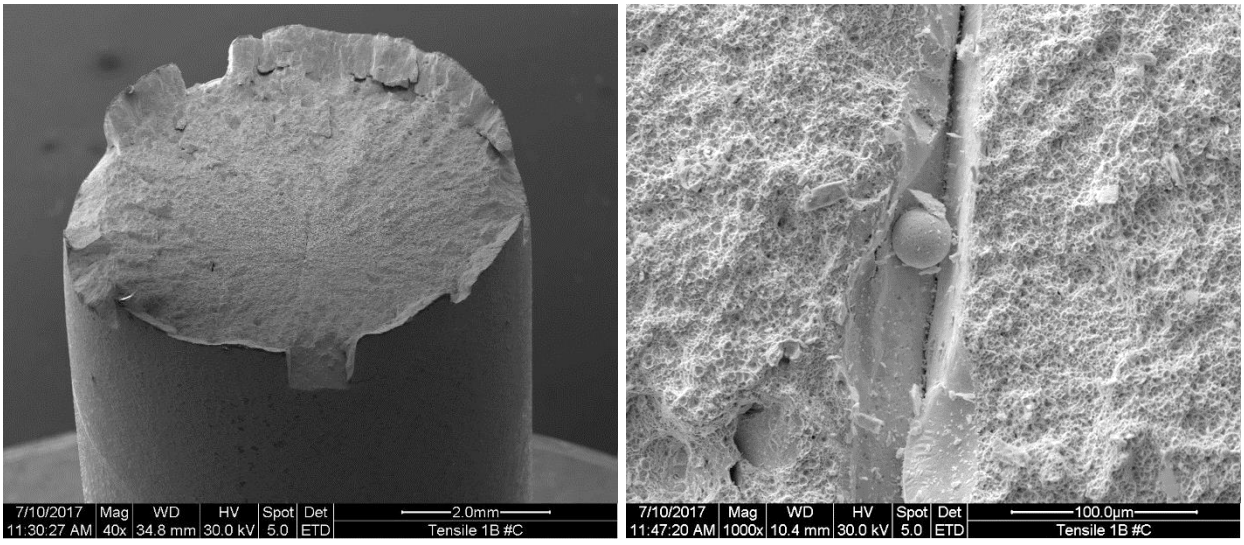

Figure 28. Electron micrographs acquired via E-SEM, 30 kV, of the failure surface of an AM U-6Nb specimen tested in the HT1 condition

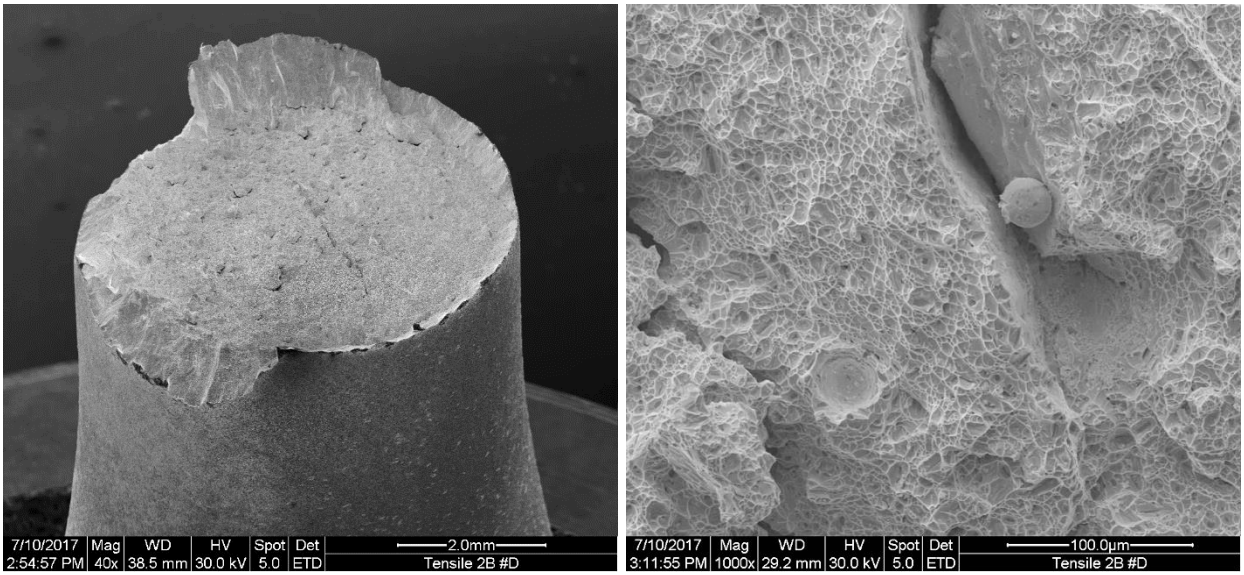

Figure 29. Electron micrographs acquired via E-SEM, 30 kV, of the failure surface of an AM U-6Nb specimen tested in the HT2 condition

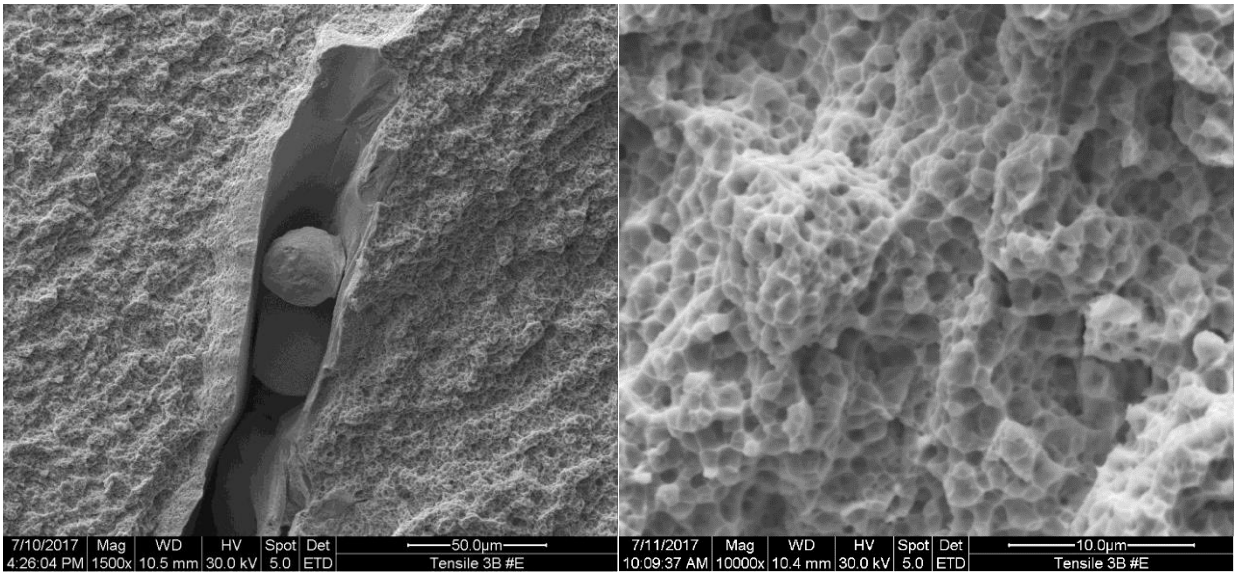

Figure 30. Higher magnification electron micrographs acquired via E-SEM, 30 kV, of the failure surface of an AM U-6Nb specimen tested in the AB condition

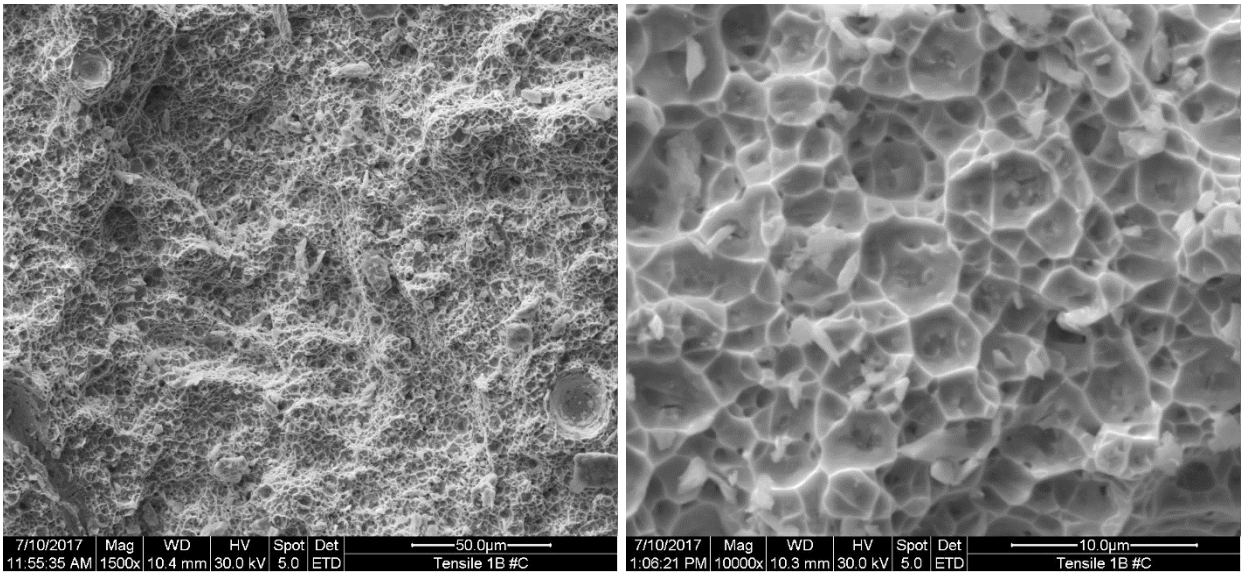

Figure 31. Higher magnification electron micrographs acquired via E-SEM, 30 kV, of the failure surface of an AM U-6Nb specimen tested in the HT1 condition

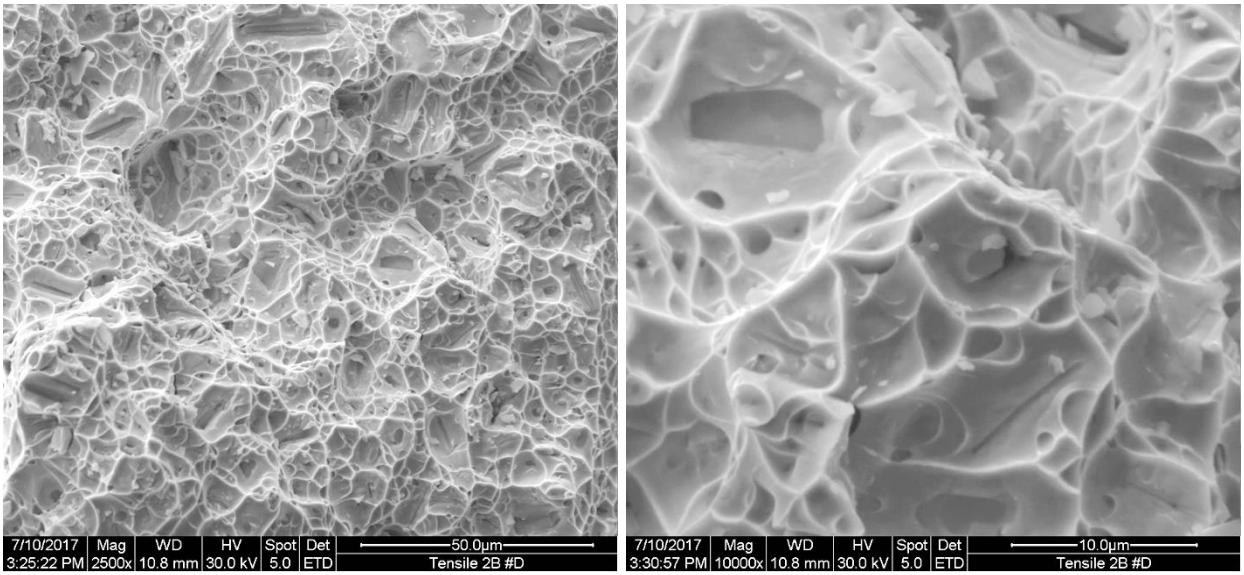

Figure 32. Higher magnification electron micrographs acquired via E-SEM, 30 kV, of the failure surface of an AM U-6Nb specimen tested in the HT2 condition

Section 7

Summary

Uranium-6 wt. pct. niobium has been melted and atomized into particles of <150 μm diameter. These particles were sieved to <100 μm diameter, then processed using laser powder bed fusion. The builds retain the U-6Nb composition, yet express multiple crystallographic phases under neutron diffraction, which is an indication of segregation during the build or cooling process. The builds are characterized by weld-like microstructures and poor ductility. To increase ductility of these builds, post build heat treatments were pursued, with quasi-static tensile behavior as the metric for potential impact.

After water quenching from the high temperature γ-BCC phase, the builds assume the α"-monoclinic phase typical of wrought or other, rapidly cooled U-6Nb. Long heat treatments result in substantially different microstructures, which evolve from melt-pool dominated to equiaxed. Evidence supporting the coarsening of inclusions is provided in the form of optical and scanning electron micrographs. These inclusions are attributed to (1) oxygen and carbon in the powder feedstock and (2) oxygen and carbon gettered during the laser powder bed fusion process, during which the powder is melted in an argon purge atmosphere. These inclusions are < 10 μm in size and are not anticipated or observed to affect machinability.

The quasi-static tensile tests performed on the annealed AM U-6Nb cylindrical dogbone specimens shows repeatable performance, with the first yield stress and ultimate tensile strength greater than standard wrought U-6Nb. The elongation is comparable, falling between 20-25%. These quasi-static mechanical properties are highly encouraging evidence toward the use of post-processing heat treatments as a means of tailoring microstructure-property behavior of U-6Nb.

This study represents a collection of experiments performed from 2016 to 2017 at Lawrence Livermore National Laboratory and Los Alamos National Laboratory. These initial investigations have highlighted the potential of U-6Nb processed using laser powder bed additive manufacturing to perform, quasi-statically, as well as wrought U-6Nb. The recommendations for process improvement, made based on the findings of this investigation include: (1) improved atmospheric control during laser powder bed fusion processing and (2) reduction of metallic impurities in powder feedstock.

Appendix A

References

1. Yemel'yanov, V.S. and A.I. Yevstyukhin, *The Metallurgy of Nuclear Fuel. Properties and Principles of the Technology of Uranium, Thorium and Plutonium*. International Series of Monographs in Nuclear Energy. Vol. 104. 1969, New York: Pergamon Press.
2. Yoshimura, H.R., J.S. Ludwigsen, M.E. McAllaster, A.J. Trennel, M.C. Brady, P.E. McConnell, K.D. Seager, K.H. Eckelmeyer, P.D. Gildea, D.M. Kim, W.L. Uncapher, and S. Wix, *Use of depleted uranium metal as cask shielding in high-level waste storage, transport, and disposal systems*. 1996, Sandia National Laboratories: Albuquerque, NM.
3. Forsberg, C.W. and M. Zucchetti, *Innovative Civilian Applications of Depleted Uranium.* Transactions of the American Nuclear Society, 2011. **105**: p. 232-233.
4. Di Benedetto, G., *Comparison of penetrator alloys for armor-piercing ammunition.* 29th International Symposium on Ballistics, Vols 1 and 2, 2016: p. 2509-2515.
5. Jackson, R.J., *Rocky Flats Technical Datasheet (RFP-1613)*, T.D.C. Company, Editor. 1971.
6. Jackson, R.J., *Metallographic study of segregation in uranium-base--niobium alloys.* Metallography, 1973. **6**(4): p. 347-360.
7. Jackson, R.J., R.P. Brugger, and D.V. Miley, *Tensile properties of gamma quenched and aged uranium-rich niobium alloys (RFP-933)*. 1967, Dow Chemical Co., Golden, Colo. Rocky Flats Div.
8. Jackson, R.J. and C.V. Kangas, *Homogenization of uranium-base niobium alloys (RFP-1582)*. 1970, Dow Chemical Co., Golden, Colo. Rocky Flats Div.
9. Eckelmeyer, K.H., *Diffusional phase-transformation in uranium alloys.* Journal of Metals, 1987. **39**(10): p. A53-A53.
10. Eckelmeyer, K.H., A.D. Romig, and L.J. Weirick, *The effect of quench rate on the microstructure, mechanical properties, and corrosion behavior of U-6 wt pct Nb.* Metallurgical Transactions A, 1984. **15**(7): p. 1319-1330.
11. Carpenter, D., A. and R. Vandermeer, A., *An X-ray diffraction study of a martensitic transformation in uranium alloys.* J. Phys. Colloques, 1982. **43**(C4): p. C4-395-C4-400.
12. Carpenter, D.A. and R.A. Vandermeer, *X-ray diffraction study of shape memory in uranium-niobium alloys.* Advances in X-Ray Analysis, 1983. **26**: p. 307-312.
13. Vandermeer, R.A., *Phase-transformations in a uranium + 14 at-percent niobium alloy.* Acta Metallurgica, 1980. **28**(3): p. 383-393.
14. Field, R.D., D.W. Brown, and D.J. Thoma, *Texture development and deformation mechanisms during uniaxial straining of U-Nb shape-memory alloys.* Philosophical Magazine, 2005. **85**(23): p. 2593-2609.
15. Vandermeer, R.A., J.C. Ogle, and W.G. Northcutt, *A phenomenological study of the shape memory effect in polycrystalline uranium-niobium alloys.* Metallurgical Transactions a-Physical Metallurgy and Materials Science, 1981. **12**(5): p. 733-741.
16. Vandermeer, R.A., J.C. Ogle, and W.B. Snyder, *Shape memory effects in a uranium + 14 at percent niobium alloy.* Scripta Metallurgica, 1978. **12**(3): p. 243-248.
17. Brown, D.W., M.A.M. Bourke, A.J. Clarke, R.D. Field, R.E. Hackenberg, W.L. Hults, and D.J. Thoma, *The effect of low-temperature aging on the microstructure and deformation of uranium-6 wt% niobium: An in-situ neutron diffraction study.* Journal of Nuclear Materials, 2016. **481**: p. 164-175.

18. Clarke, A.J., R.D. Field, R.E. Hackenberg, D.J. Thoma, D.W. Brown, D.F. Teter, M.K. Miller, K.F. Russell, D.V. Edmonds, and G. Beverini, *Low Temperature Age Hardening in U-13 at.% Nb: An Atom Probe Tomography Study.* Journal of Nuclear Materials, 2009. **393**(2): p. 282-291.
19. Clarke, A.J., R.D. Field, R.J. Mc Cabe, D.W. Brown, B. Clausen, P.O. Dickerson, C.M. Cady, R.E. Hackenberg, D.J. Thoma, J.G. Swadener, and C.N. Tupper, *Shape memory effect deformation structures in U-14at.%Nb: polycryalline and single crystal behavior*. Conference: International Symposium on Plasticity 2012 and its Current Applications ; January 3, 2012 ; San Juan, Puerto Rico. 2011: ; Los Alamos National Laboratory (LANL). Medium: ED.
20. Field, R.D., C.N. Tome, R.J. Mc Cabe, A.J. Clarke, D.W. Brown, and C.N. Tupper, *Deformation of the U-14at%Nb shape memory alloy experiments and modeling*. TMS 2011 Annual Meeting. 2011, San Diego, CA: Los Alamos National Laboratory (LANL).
21. Hackenberg, R.E., G.M.S. Hemphill, R.T. Forsyth, P.A. Papin, A.M. Kelly, T.J. Tucker, R.M.J. Aikin, D.J. Alexander, M.F. Lopez, and A.J. Clarke, *Unraveling the Age Hardening Response in U-Nb Alloys (LA-UR-16-20301).* Materials Science Forum (Online), 2016: p. 665-670.
22. Hackenberg, R.E. and G.M. Hemphill, *Property and lifetime prediction in aged U-Nb alloys: a statistical assessment (LA-14389).* 2009, ; Los Alamos National Laboratory (LANL), Los Alamos, NM. p. Medium: ED; Size: 743 KB.
23. Hackenberg, R.E., G.M. Hemphill, D.J. Alexander, T.J. Tucker, R.M.J. Aikin, and R.T. Forsyth, *U-Nb Aging and Lifetime Prediction: Assessment for 2012 (LA-UR-12-26893).* 2012, Los Alamos National Laboratory (LANL).
24. Brown, D.W., M.A.M. Bourke, P.S. Dunn, R.D. Field, M.G. Stout, D.F. Teter, D.J. Thoma, and S.C. Vogel, *Asymmetric lattice response during tensile and compressive deformation of a uranium-niobium shape memory alloy*, in *Neutron and X-Ray Scattering as Probes of Multiscale Phenomena*, S.R. Bhatia, et al., Editors. 2005, Materials Research Soc: Warrendale. p. 205-210.
25. Brown, D.W., M.A.M. Bourke, P.S. Dunn, R.D. Field, M.G. Stout, and D.J. Thoma, *Uniaxial tensile deformation of uranium 6 wt pct niobium: A neutron diffraction study of deformation twinning.* Metallurgical and Materials Transactions a-Physical Metallurgy and Materials Science, 2001. **32**(9): p. 2219-2228.
26. Brown, D.W., M.A.M. Bourke, R.D. Field, W.L. Hults, D.F. Teter, D.J. Thoma, and S.C. Vogel, *Neutron diffraction study of the deformation mechanisms of the uranium-7 wt.% niobium shape memory alloy.* Materials Science and Engineering a-Structural Materials Properties Microstructure and Processing, 2006. **421**(1-2): p. 15-21.
27. Tupper, C.N., D.W. Brown, R.D. Field, T.A. Sisneros, and B. Clausen, *Large Strain Deformation in Uranium 6 Wt Pct Niobium.* Metallurgical and Materials Transactions a-Physical Metallurgy and Materials Science, 2012. **43A**(2): p. 520-530.
28. Cady, C.M., G.T. Gray, S.R. Chen, E.K. Cerreta, C.P. Trujillo, M.F. Lopez, R.M. Aikin, D.R. Korzekwa, A.M. Kelly, and Edps, *The mechanical response of a Uranium-Niobium alloy: A comparison of cast versus wrought processing*. Dymat 2009: 9th International Conference on the Mechanical and Physical Behaviour of Materials under Dynamic Loading, Vol 2. 2009, Cedex A: E D P Sciences. 1045-+.
29. Wu, A.S., D.W. Brown, B. Clausen, and J.W. Elmer, *The influence of impurities on the crystal structure and mechanical properties of additive manufactured U-14 at.% Nb.* Scripta Materialia, 2017. **130**: p. 59-63.
30. Sunwoo, A.J., T.S. Chow, and C.J. Long, *Effect of physical vapor deposition on microstructure and properties of uranium 6 wt% niobium alloy.* Journal of Nuclear Materials, 1998. **254**(1): p. 65-73.
31. Aikin Jr., R.M., C.M. Cady, S.-R. Chen, E.K. Cerreta, G.T. Gray III, C.P. Trujillo, M.F. Lopez, and D.R. Korzekwa, *Characterization of a direct cast U-6wt%Nb part (LA-UR-09-02856).* 2009, Los Alamos National Laboratory: Los Alamos NM.

32. Sun, S., M. Brandt, and M. Easton, *Powder bed fusion processes: An overview*, in *Laser Additive Manufacturing Materials, Design, Technologies and Applications*, M. Brandt, Editor. 2017, Woodhead Publishing. p. 55-77.
33. Mercelis, P. and J.-P. Kruth, *Residual stresses in selective laser sintering and selective laser melting.* Rapid Prototyping Journal, 2006. **12**(5): p. 254-265.
34. Wu, A.S., D.W. Brown, M. Kumar, G.F. Gallegos, and W.E. King, *An Experimental Investigation into Additive Manufacturing-Induced Residual Stresses in 316L Stainless Steel.* Metallurgical and Materials Transactions A, 2014. **45**(13): p. 6260-6270.
35. Murr, L.E., *Metallurgy of additive manufacturing: Examples from electron beam melting.* Additive Manufacturing, 2015. **5**(Supplement C): p. 40-53.
36. Zhu, Y., X. Tian, J. Li, and H. Wang, *The anisotropy of laser melting deposition additive manufacturing Ti–6.5Al–3.5Mo–1.5Zr–0.3Si titanium alloy.* Materials & Design, 2015. **67**(Supplement C): p. 538-542.
37. Thijs, L., M.L. Montero Sistiaga, R. Wauthle, Q. Xie, J.-P. Kruth, and J. Van Humbeeck, *Strong morphological and crystallographic texture and resulting yield strength anisotropy in selective laser melted tantalum.* Acta Materialia, 2013. **61**(12): p. 4657-4668.
38. Popovich, V.A., E.V. Borisov, A.A. Popovich, V.S. Sufiiarov, D.V. Masaylo, and L. Alzina, *Functionally graded Inconel 718 processed by additive manufacturing: Crystallographic texture, anisotropy of microstructure and mechanical properties.* Materials & Design, 2017. **114**(Supplement C): p. 441-449.
39. McKeown, J.T., L.L. Hsiung, J.M. Park, H.J. Ryu, P.E.A. Turchi, and W.E. King, *Size-dependent microstructures in rapidly solidified uranium niobium powder particles.* Journal of Nuclear Materials, 2016. **479**: p. 1-10.
40. McKeown, J.T., L.L. Hsiung, H.J. Ryu, J.M. Park, P.E.A. Turchi, and W.E. King, *Rapidly solidified U–6wt%Nb powders for dispersion-type nuclear fuels.* Journal of Nuclear Materials, 2014. **448**(1): p. 72-79.
41. Thijs, L., F. Verhaeghe, T. Craeghs, J.V. Humbeeck, and J.-P. Kruth, *A study of the microstructural evolution during selective laser melting of Ti–6Al–4V.* Acta Materialia, 2010. **58**(9): p. 3303-3312.
42. International, A., *Standard Test Methods for Tension Testing of Metallic Materials*, in *ASTM E8/E8M-16a*. 2016, ASTM International West Conshohocken PA.
43. Peterson, N.L. and R.E. Ogilvie, *Diffusion in the uranium-niobium (Columbium) system.* Transactions of the Metallurgical Society of AIME, 1963. **227**: p. 1083-1087.
44. King, W.E., H.D. Barth, V.M. Castillo, G.F. Gallegos, J.W. Gibbs, D.E. Hahn, C. Kamath, and A.M. Rubenchik, *Observation of keyhole-mode laser melting in laser powder-bed fusion additive manufacturing.* Journal of Materials Processing Technology, 2014. **214**(12): p. 2915-2925.
45. Zhao, C., K. Fezzaa, R.W. Cunningham, H. Wen, F. De Carlo, L. Chen, A.D. Rollett, and T. Sun, *Real-time monitoring of laser powder bed fusion process using high-speed X-ray imaging and diffraction.* Scientific Reports, 2017. **7**(1): p. 3602.
46. Mukherjee, T., J.S. Zuback, A. De, and T. DebRoy, *Printability of alloys for additive manufacturing.* Scientific Reports, 2016. **6**: p. 19717.
47. Bourke, M.A.M., D.C. Dunand, and E. Ustundag, *SMARTS - a spectrometer for strain measurement in engineering materials.* Applied Physics a-Materials Science & Processing, 2002. **74**: p. S1707-S1709.
48. Von Dreele, R.B., J.D. Jorgensen, and C.G. Windsor, *Rietveld refinement with spallation neutron powder diffraction data.* Journal of Applied Crystallography, 1982. **15**(6): p. 581-589.
49. Larson and R.B. Von Dreele, *General Structure Analysis System (LA-UR-86-748)*. 1986, Los Alamos National Laboratory.
50. Parikh, H.M., D.K. Adamson, and T.B. Tjader, *IGF analysis of U-6Nb powder and solid material*. 2016, Y-12 National Security Complex.

51. Wu, A.S. and M. Iniguez, *Effect of build location on oxygen content in specimens processed using SLM and Concept Laser M2 chambers (Internal Report)*. 2017.
52. Hsiung, L.L. and G.H. Campbell, *Microstructural Characterization and Heat-Treatment Optimization for the Development of AM U-6wt.%Nb Alloy Part One: Microsegregation and Microstructural Inhomogeneity (LLNL-TR-713757)*. 2016, Lawrence Livermore National Laboratory: Livermore CA.
53. Field, R.D., D.J. Thoma, P.S. Dunn, D.W. Brown, and C.M. Cady, *Martensitic structures and deformation twinning in the U–Nb shape-memory alloys.* Philosophical Magazine A, 2001. **81**(7): p. 1691-1724.
54. Zhao, J.C., L.A. Peluso, M.R. Jackson, and L. Tan, *Phase diagram of the Nb–Al–Si ternary system.* Journal of Alloys and Compounds, 2003. **360**(1): p. 183-188.
55. Hall, E.O., *The Deformation and Ageing of Mild Steel: III Discussion of Results.* Proceedings of the Physical Society. Section B, 1951. **64**(9): p. 747.
56. Hansen, N., *Hall–Petch relation and boundary strengthening.* Scripta Materialia, 2004. **51**(8): p. 801-806.
57. Yue, T.M., H.U. Ha, and N.J. Musson, *Grain size effects on the mechanical properties of some squeeze cast light alloys.* Journal of Materials Science, 1995. **30**(9): p. 2277-2283.
58. Hackenberg, R.E., D.W. Brown, A.J. Clarke, L.B. Dauelsberg, R.D. Field, W.L. Hults, A.M. Kelly, M.F. Lopez, D.F. Teter, D.J. Thoma, T.J. Tucker, C.J. Vigil, and H.M. Volz, *U-Nb aging final report (LA-14327)*. 2007, Los Alamos National Laboratory: Los Alamos NM.